TEXS: in-vacuum tender X-ray emission spectrometer with 11 Johansson crystal analyzers

Mauro Rovezzi, Alistair Harris, Blanka Detlefs, Timothy Bohdan, Artem Sviazhin, Alessandro Santambrogio, David Degler, Rafal Baran, Benjamin Reynier, Pedro Noguera Crespo, et al.

TEXS: in-vacuum tender x-ray emission spectrometer based on eleven Johansson crystal anlysers

MAURO ROVEZZI,[a,b]* ALISTAIR HARRIS,[c] BLANKA DETLEFS,[b] TIMOTHY BOHDAN,[b] ARTEM SVIAZHIN,[b] ALESSANDRO SANTAMBROGIO,[b] DAVID DEGLER,[b] RAFAL BARAN,[b] BENJAMIN REYNIER,[b] PEDRO NOGUERA CRESPO,[d] CATHERINE HEYMAN,[c] HANS-PETER VAN DER KLEIJ,[b] PIERRE VAN VAERENBERGH,[b] PHILIPPE MARION,[b] HUGO VITOUX,[b] CHRISTOPHE LAPRAS,[b] ROBERTO VERBENI,[b] MENHARD MENYHERT KOCSIS,[b] ALAIN MANCEAU[e] AND PIETER GLATZEL [b]*

[a]*Univ. Grenoble Alpes, CNRS, IRD, Irstea, Météo France, OSUG, FAME, 71 avenue des Martyrs, CS 40220, 38043, Grenoble, France,* [b]*European Synchrotron Radiation Facility, 71 avenue des Martyrs, CS 40220, 38043 Grenoble, France,* [c]*Design et Mécanique, Les Coings, 38210, Montaud, France,* [d]*Added Value Solutions (AVS), Pol. Ind. Sigma Xixilion Kalea 2, Bajo Pabellón 10, 20870 Elgoibar, Spain, and* [e]*ISTerre, Université Grenoble Alpes, CNRS, CS 40700, 38058 Grenoble, France. E-mail: mauro.rovezzi@esrf.fr, glatzel@esrf.fr*

X-ray instrumentation; Wavelength dispersive spectrometer; X-ray optics; Tender x-rays; Johansson crystal analysers

Abstract

Version 0.2.47.1 We describe the design and show first results of a large solid angle x-ray emission spectrometer that is optimised for energies down to 1.5 keV. The spectrometer is based on an array of eleven cylindrically bent Johansson crystal analysers arranged in a

point-to-point Rowland circle geometry. The smallest achievable energy bandwidth is equal or smaller than the core hole lifetime broadening of the absorption edges in this energy range. Energy scanning is achieved using an innovative design, maintaining the Rowland circle conditions for all crystals using only four motor motions. The entire spectrometer is encased in a high-vacuum chamber that allows use of a liquid Helium cryostat and provides sufficient space for *in situ* cells or *operando* catalysis reactors.

1. Introduction

X-ray emission x-ray spectroscopy is attracting growing interest as a tool to characterise local electronic and atomic structure. We define emission spectroscopy as recording the emitted x-rays from a fluorescence source with an energy bandwidth that is on the order of the core hole lifetime broadening. The spectroscopic techniques with such an instrument include non-resonant x-ray emission spectroscopy (XES) that does not require a monochromatic incoming beam to excite the analyte atom as well as resonant inelastic x-ray scattering (RIXS) and high energy resolution fluorescence detected (HERFD) x-ray absorption near edge structure (XANES) spectroscopy that are usually carried out on x-ray spectroscopy beamlines at synchrotron radiation sources. A series of books and review papers describes the applications of XES, RIXS and HERFD-XANES in solid state physics, materials science, coordination chemistry and biology (Meisel *et al.*, 1989; Glatzel & Bergmann, 2005; Rueff & Shukla, 2013; Hayashi, 2000; Rovezzi & Glatzel, 2014; Bauer, 2014; Sa, 2014; DeBeer & Bergmann, 2016; Proux *et al.*, 2017). More performing and user-friendly x-ray emission spectrometers at synchrotron radiation facilities and in the laboratory, combined with tools for theoretical interpretation of the data, have greatly helped the adoption of the techniques by a large community.

The x-ray energy range between 1.5 keV and 5.5 keV, the so-called “tender” x-ray range, covers the K absorption edges of Al to Cl, the L-edges of 4*d* transition metals and the M-edges

of $5d$ transition metals, lanthanides and actinides. The chemical sensitivity of fluorescence lines can be used to characterise the electronic structure and local coordination (Alonso Mori *et al.*, 2009; Mori *et al.*, 2010). It is very attractive for heavy elements to use absorption edges of shallow instead of deep core holes (*e.g.* L- instead of K-edge for $4d$ transition metals) because of the greatly reduced spectral broadening arising from the core hole lifetime. This has recently been exploited in high pressure and magnetism (Wilhelm *et al.*, 2016) research or applications in chemistry and catalysis (Thompson *et al.*, 2015). The spectral broadening can be further reduced by using an x-ray emission spectrometer for recording the fluorescence lines instead of a conventional solid state detector. So far, this approach has been applied in the field of catalysis (Thomas *et al.*, 2015), Li–S batteries (Kavčič *et al.*, 2016) and actinides chemistry (Kvashnina *et al.*, 2013; Kvashnina *et al.*, 2019).

Despite its relevance, the tender x-ray range is rarely exploited using high energy resolution techniques because of technical challenges. First of all, the low energies require vacuum conditions in order to minimise absorption by air. Furthermore, the high energy resolution can be achieved either with wavelength dispersive optics or detectors that use materials in their superconducting state (Doriese *et al.*, 2017). Wavelength dispersive optics can be realised using either gratings or perfect crystals. As the efficiency of gratings decreases rapidly towards higher energies, perfect crystals are generally used in tender x-ray spectrometers. Historically, soft crystals with large *d*-spacing were employed for this energy range, such as Lithium Fluoride (LiF), Pentaerythritol (PET), Thallium Acid Phthalate (KAP), Pb Stearate or micas. Unfortunately, those crystals are not stable with time and under intense x-ray irradiation. Thus, standard high-quality hard crystals such as Silicon (Si), Germanium (Ge) or Quartz (β-SiO_2) are preferred.

X-ray emission spectrometers can generally be grouped into point-to-point focusing and dispersive geometries. The main difference is in the way the captured solid angle (*i.e.* the total crystal surface) is partitioned. A point-to-point geometry aims to minimise the angular

spread $\Delta\theta$ given by the entire solid angle. This is realised in the Rowland geometry with sample, crystal surface and detector placed on the Rowland circle. A spectrum is recorded by rotating and displacing the crystal optics in order to change the Bragg angle. The angular spread translates into the energy bandwidth of the instrument. In a dispersive setup, the Bragg angle changes over the crystal surface and the x-rays are reflected onto a position sensitive detector. A prominent example is the von Hamos geometry (Hoszowska *et al.*, 1996; Dousse & Hoszowska, 2014). In this case, a spectrum can be recorded in a stationary configuration. We note that there are hybrid instruments that work in point-to-point focusing with dispersion correction (Welter *et al.*, 2005; Huotari *et al.*, 2006; Holden *et al.*, 2017). An important application for the instrument presented here is HERFD-XANES in samples with low analyte concentration. In this case, the captured solid angle must be used in the smallest possible energy window. Consequently, a point-to-point focusing geometry was chosen. The interested reader may refer to the excellent work by Wittry and Li (Wittry & Li, 1993) for a quantitative comparison of scanning spectrometers *versus* dispersive setups.

Reviewing all existing instruments is well beyond the scope of this manuscript. We may only underline that to further increase the collected effective solid angle, a multi-analyser configuration is usually adopted. While this strategy is well established for hard x-rays, it has not been realised yet for the tender x-ray energy range. In fact, existing instruments at this energy range are based on a single analyser (Kavčič *et al.*, 2012; Abraham *et al.*, 2019).

The manuscript is organised as follows. In Section 2 the concept design is given. The mechanical design and description of the produced instrument are reported in Section 3. Finally, the results and performances obtained from the commissioning phase are reported and discussed in Section 4.

2. Concept design

The concept design of the spectrometer is based on the following specifications: 1) energy range between 1.5 keV and 5.5 keV, continuously covered with standard high quality crystals, *e.g.* Si, Ge and β-SiO_2; 2) energy bandwidth close or below the core-hole lifetime broadening of the emission lines measured; 3) optimised solid angle per energy bandwidth, that is, a Rowland circle diameter $\leq$1 m and multi-analyser configuration; 4 windowless from the ultra-high vacuum of the host beamline down to the detector, in order to minimise x-ray attenuation.

Three sets of crystal cuts, β-SiO_2(100), Si(111) and Si(220), are required to continuously cover the 1.5–5.5 keV energy range. The Bragg angle (θ_B) ranges from 85° to 35°, as shown in Figure 1. The elements and emission lines accessible in this range are also reported in Figure 1, where for simplicity only the Kα_1, Lα_1 and Mα_1 lines are shown. The Rowland geometry (Rowland, 1882) used for the design of the spectrometer is shown in Figure 2. The points representing the sample (O), crystal analyser (C) and detector (D) define a circle, the Rowland circle with a diameter R. The plane containing the Rowland circle defines the meridional or dispersive direction. In a symmetric geometry the source-to-analyser (OC) and the analyser-to-detector (CD) distances are equal. Furthermore, the Rowland circle is rotated about the X axis such that the centre of the analyser crystal is at Z=0 for all Bragg angles as shown in the bottom panel of Figure 2. The scattering plane (XY) contains the incoming x-ray beam and the centre of the crystal. The source volume is given by the point where the incoming x-rays impinge on the sample surface. The scattering geometry is important if the radiation emitted by the sample is not isotropic. This is the case, *e.g.*, for elastic and Compton scattering that give rise to background in the energy range of the fluorescence lines. For horizontal linear polarised light it is thus advantageous to align the spectrometer normal to the incoming beam (X) and on the scattering plane (as is represented in Figure 2). This explains why we chose to have the crystal analyser at Z=0 for all Bragg angles. Another reason is the fixed angle of view towards the sample, which is important for *in situ* and *operando* cells

Figure 1: Angular range of the spectrometer with standard reflections. The elements and corresponding energies of three selected families of emission lines, namely, Kα_1, Lα_1 and Mα_1, are indicated in the top axes. The dashed vertical lines are a guide for the eye for Kα_1 and Lα_1 lines.

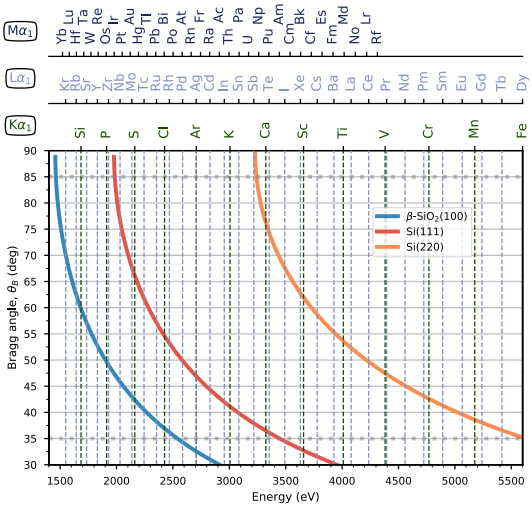

or cryostats with a limited window opening. In summary, the chosen configuration minimises the elastic scattering and keeps the angle of view to the sample constant with respect to the central crystal. We note that when more crystals are added (see below) only the central crystal remains at Z=0 while the other crystals have to move in Z. This is the results of the condition of using one x-ray detector. The displacement in Z is small and our arguments above still apply. One could imagine a design where each crystal has its own detector that moves independently of the others. However, that is mechanically extremely difficult to realise.

The sagittal plane is perpendicular to the sample-detector axis (OD). It is inclined by $\frac{\pi}{2} - \theta_B$ with respect to the scattering plane. A rotation of the Rowland circle around the sample-detector axis describes a circle on the sagittal plane with radius R$\cdot \sin(\theta_B)^2$, which we call the sagittal circle. Each point on this circle thus forms a Rowland circle containing points O and D and O$\hat{\text{C}}$D angle $\pi - 2\theta_B$. This is the condition for dynamical sagittal focusing as it depends on the Bragg angle. This could be realised by dynamically bending a crystal wafer. However, this would lead to anticlastic bending in the meridional direction. The solution is a segmentation of the crystals in the sagittal direction. The smaller the segments the better

Figure 2: Rowland circle geometry employed for the instrument design: a generic doubly-bent diffractor (top); how the crystal analyser and detector move on the Rowland circle when changing the Bragg angle (bottom). Dimensions are not in scale.

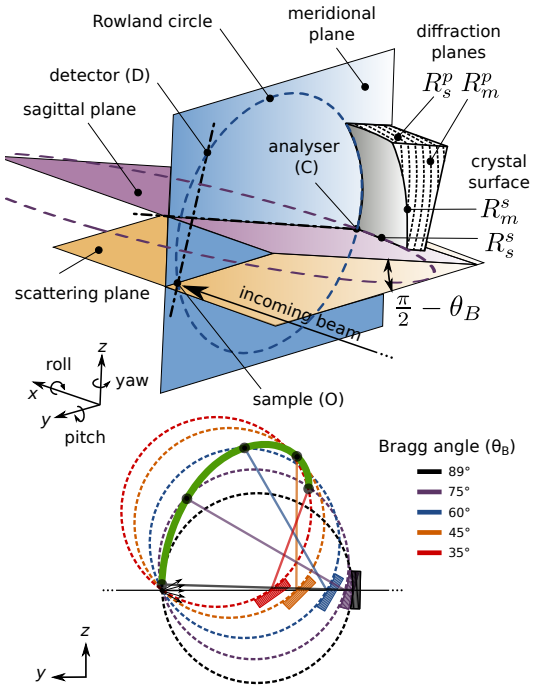

is the approximation to the correct sagittal bending radius. Our choice was to use an array of eleven cylindrical Johansson crystal analysers with fixed shape and dynamically placed on the sagittal circle. This choice was governed by the availability of Johansson crystals and ultimately costs. The concept we describe in the following can be further developed for more segments and/or smaller crystal bending radii.

The optimisation of the performances for a generic doubly bent crystal analyser is based on an analytical study, as performed by Wittry and Sun (Wittry & Sun, 1990*b*; Wittry & Sun, 1990*a*; Wittry & Sun, 1991; Wittry & Sun, 1992). It consists in calculating analytically the $\Delta\theta(x, z)$ distribution over the area of the crystal analyser as a function of the Bragg angle θ_B. Each analyser is defined by four bending radii: R^s_m, R^p_m, R^s_s, R^p_s which are the bending radius of the surface (R^s) and crystal planes (R^p) in the meridional direction (R_m) or sagittal direction (R_s). To take into account the limited bandwidth of the fluorescence line of interest, ΔE, a θ-dependent threshold in $\Delta\theta$ is established using the differential form of the Bragg equation, $|\Delta E/E| = \Delta\theta/\tan\theta$. For example, Sulphur K$\alpha_1$ has an intrinsic line width ΔE = 0.61 eV at E = 2307.8 eV, as tabulated in XRAYLIB (Schoonjans *et al.*, 2011). With Si(111) this energy corresponds to θ = 58.95°. The angular spread of this line is then $\Delta\theta = 4.3 \times 10^{-4}$ rad. We chose a ΔE threshold of 0.5 eV. The results are shown in Figure 3. An "effective solid angle per energy bandwidth" as a function of the Bragg angle and for a given type of crystal analyser was calculated. We included in the study only those crystal analysers geometries based on well established production technologies: 1) spherically bent crystal analysers, SBCAs – for a recent overview (Rovezzi *et al.*, 2017) and references therein; 2) cylindrically bent Johansson crystal analysers, CBJCAs (Johansson, 1933). SBCAs are widely used on hard x-ray instruments where it is possible to work in back-scattering conditions (θ_B close to 90°). CBJCAs are mainly developed as x-ray optics for laboratory diffractometers with the goal to monochromatise the x-ray tube source, *e.g.* selecting only the Kα_1 emission line, and usually working in grazing-incidence asymmetric conditions.

Figure 3: Effective scattering area for a spherical and a Johansson analyser (*cf.* main text).

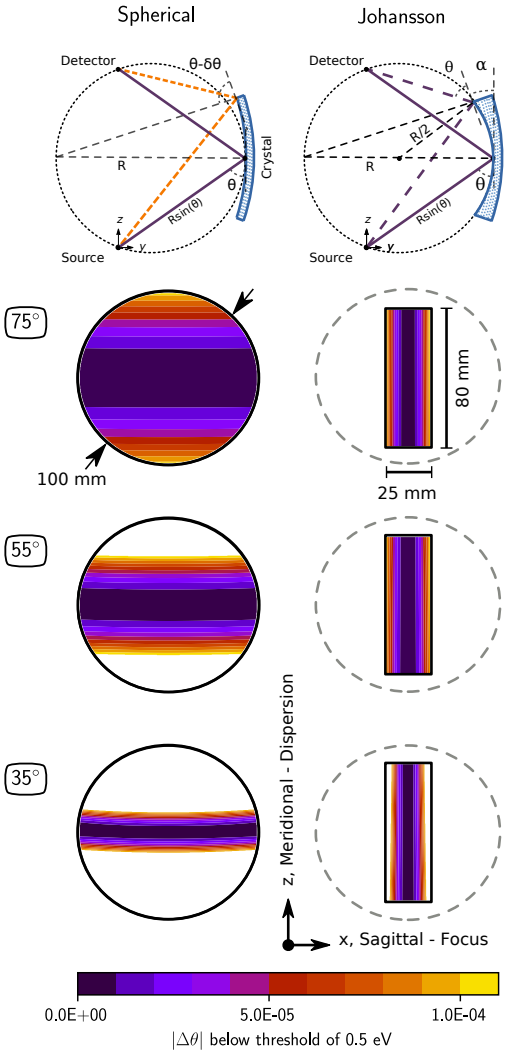

The main differences between SBCAs and CBJCAs are shown in Figure 3. We consider first the meridional/dispersive direction. SBCAs are built by bending a thin crystalline wafer (typically Si or Ge of ≈100 μm) on a spherical substrate of circular shape (typically 100 mm diameter) and radius R, the diameter of the Rowland circle. As a consequence, all four radii are equal, $R^{s,p}_{m,s}$ = R. A chromatic aberration ($\delta\theta$) is introduced when moving out of the centre of the crystal. This aberration, also know as Johann error, scales with $1/\tan\theta_B$ and becomes prohibitive for small Bragg angles. Assuming a threshold of 0.5 eV we show in Figure 3 that a decreasing area of the analyser contributes to the scattered amplitude for $\theta_B < 75°$. This aberration is removed in CBJCAs. In fact, the Johansson analyser is manufactured via a bending plus grinding process (*cf.* Section 4.1). It results in R^p_m = R and R^s_m = R/2. This condition ensures identical Bragg over the crystal surface in the meridional direction because the crystal planes have a variable miscut angle $\alpha = \frac{1}{2}\arcsin(\frac{l}{\mathrm{R}})$, where l is the distance from the centre of the analyser. Without chromatic aberration the CBJCAs efficiently scatter also for Bragg angles below 75°.

Regarding the sagittal direction, the ideal condition would require R^s_s = R^p_s = R $\sin(\theta_B)^2$. SBCAs are superior to CBJCAs because of the double bending. In fact, CBJCAs are flat in this direction (R^s_s = R^p_s = ∞) and for this reason suffer a chromatic aberration that has a second order dependency on the Bragg angle. For a point source, $\Delta\theta = \tan\theta\left(1\Big/\sqrt{1+(\frac{w}{2\mathrm{R}\sin\theta})^2}-1\right)$, where w is the width of the flat side. This disadvantage can be corrected relatively easily by reducing the size of each analyser in the sagittal direction and increasing the number of analysers in the spectrometer. With the given threshold of 0.5 eV, it is found that a width of 25 mm keeps the full efficiency of the analyser for the whole angular range. Furthermore, considering the current limitations in CBJCAs production process based on 100 mm diameter Si wafers, the size in the meridional direction is reduced to 80 mm, allowing two analysers per wafer.

Two additional non-negligible factors that contribute to the energy broadening are: 1) the finite source size, given by the footprint of the exciting radiation (x-rays or particles) on

the sample; 2) the strain and defects introduced in the analyser crystal lattice by the bending and grinding. To correctly take into account these two effects, the previous analytical study is complemented by ray tracing calculations. The simulations were carried out using the SHADOW3 (Sanchez del Rio *et al.*, 2011) code for a cylindrically-bent Johansson-type crystal analyser with rectangular shape of 25 mm (sagittal) and 80 mm (meridional). Two bending radii, 1 m and 0.5 m, were considered for each of Si(111) and Si(220) analysers. The simulations assume an elliptical source of 0.1 mm (vertical, Z) and 0.5 mm (horizontal, X) and also consider the distortion of the crystal planes by the strain induced by the bending using the multilamellar model (Sanchez del Rio *et al.*, 2015). The tabulated energy widths of the Kα_1 (K-L_3), Lα_1 (L_3-M_5) and Mα_1 (M_5-N_6) lines for all the elements accessible in the covered energy range are given for a comparison with the expected performances. The results are summarised in Figure 4. When studying L- or M-edges both 0.5 m or 1 m configurations offer an experimental energy broadening below the width of the emission lines. For the K-edges of light elements or when the highest energy resolution is required, a configuration with 1 m bending radius is preferred. Nevertheless, for those applications focused on HERFD-XANES, mainly requiring high detection efficiency, the 0.5 m bending radius configuration would be an asset.

A schematic view of the final concept design is given in Figure 5 for the two extreme angular positions of the spectrometer, namely, 85° and 35°. The sample and the incoming beam exciting the source for the analysers are laying on the horizontal plane, while the analysers reside on the sagittal plane, whose inclination depends on the Bragg angle. The eleven analysers at R=500 mm cover a solid angle ranging from 50 msr (θ_B =35°) up to 87 msr (θ_B =85°). About a factor four less is covered when R=1000 mm.

Figure 4: Results of the ray tracing study for a Si CBJCA of 25×80 mm^2 size plus an elliptical fluorescence source size of 0.1×0.5 mm^2 (*cf.* main text). The tabulated width of the emission lines for all the elements accessible in the given energy range are reported for comparison. The top scales give the corresponding Bragg angle for Si(111) and Si(220) reflections.

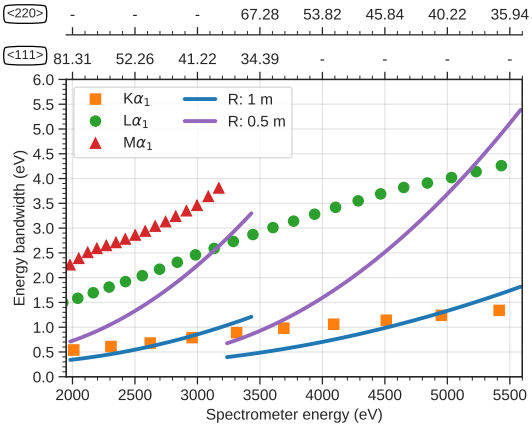

3. Mechanical design and production

This section presents the mechanical design of the spectrometer as built and installed in the first experimental hutch of the beamline ID26 of the ESRF. The instrument was manufactured, assembled and tested by the company Added Value Solutions (Spain).

X-ray attenuation by air and windows is strong in the tender energy range. 1 cm of air or 8 μm of Kapton absorb, respectively, 50% and 40% of x-rays at 2 keV. For this reason, a fully in vacuum solution was adopted. The whole spectrometer mechanics and sample environment are encased in a vacuum vessel of ≈4 m^3, roughly, a cylinder of 1.74 m diameter and 1.67 m height, as shown in Figure 6A. The vacuum vessel has an optimised shape for a complete movement on the scanning trajectories of the crystal analysers with a bending radius ranging from 1020 mm down to 480 mm and the x-ray detector. The vacuum level is below 1×10^{-5} mbar. It allows connecting the spectrometer directly to the ultra-high vacuum of the host beamline - via a differential pumping system - and is sufficient for thermal insulation, allowing the use of a windowless liquid Helium cryostat (*cf.* section 3.3). The required vacuum level is obtained by introducing only high vacuum compatible components and avoiding trapped volumes. The obtained out-gassing rate is 3×10^{-10} mbar·L/s/cm^2, comparable to un-

Figure 5: Overview of the concept design at two extreme Bragg angles.

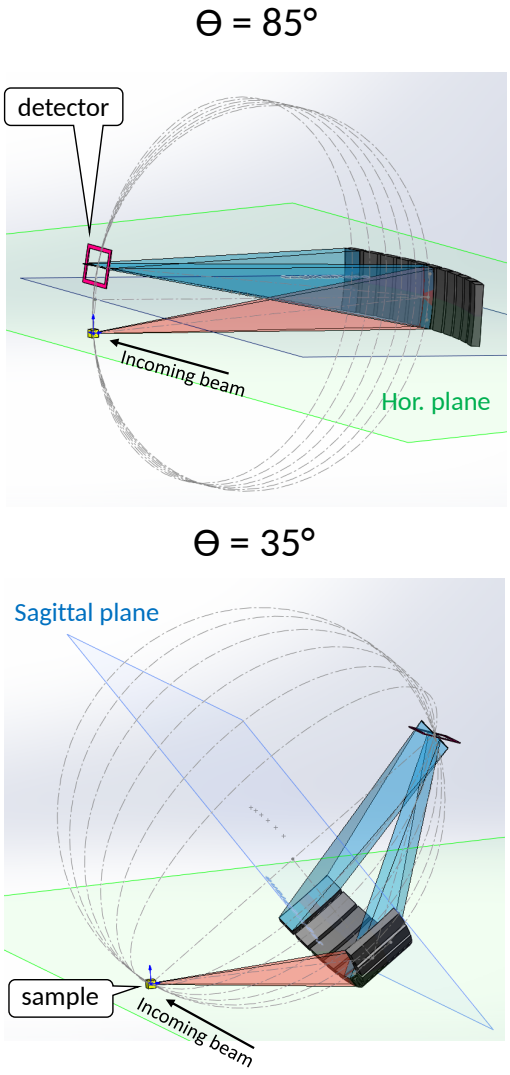

baked stainless steel after 24h of pumping. Primary and turbo pumps are mounted on a CF 250 port. The pumping capacity is 80 m^3/h (Leybold Leyvac 80 dry compressing pump) and 2100 l/s (Turbovac MagW 2200iP turbomolecular magnetically levitated pump). Via this system, the pumping time is approximately 90 minutes to reach the low 10^{-5} mbar range. The spectrometer is operated in vacuum during the experiment and the sample exchange is performed via a load lock system (*cf.* section 3.3). Installation of an *in situ* cell is possible by inverse vacuum setups and feedthroughs in the available chamber ports.

The spectrometer accounts a total of fifty-two motorised axes controlled by the BLISS software (Guijarro & others, 2018) via IcePap stepper motor drivers. The exact Rowland circle tracking is achieved via a device server implemented in Python (Rovezzi, 2017). Critical motor axes are equipped with absolute encoders. The vacuum vessel is mounted on a motorised long rail. It allows aligning the origin of the spectrometer along the Y direction, perpendicular to the incoming x-ray beam in the horizontal plane and move the whole spectrometer in a "maintenance mode", when disconnected from the beamline. The whole spectrometer is isolated from the vacuum vessel via an externally motorised four-point lifting system plus two ball-screw guiding columns connected to the vacuum only via edge-welded bellows. This system allows aligning the spectrometer along the Z direction and avoids transmitting vibrations from ground to the mechanics. The structural analysis performed via finite elements calculations confirms that the vibration modes do not act in the direction of interest, that is, directly affecting the Bragg angle. The first main mode consists on a global lateral oscillation along X with a maximum displacement of 0.4 mm and a frequency of 16.3 Hz. This mode does not affect the energy resolution as the whole spectrometer oscillates around the incoming beam focal point.

The spectrometer frame consists of a welded stainless steel structure divided in three main sub-assemblies (*cf.* Figure 6B): the crystal analyser cradle (1); the detector arm (2); sample tower (3). These components are described in details in the following sub-sections.

Figure 6: Layout of the spectrometer (*cf.* main text).

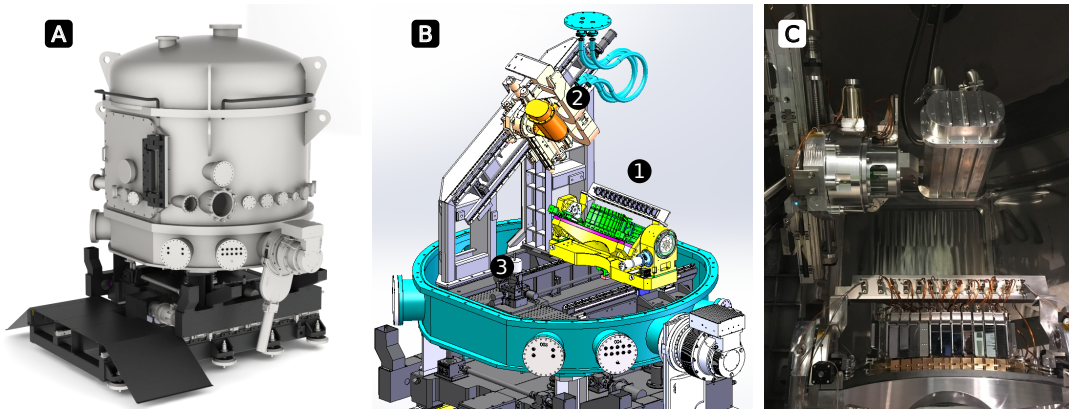

3.1. Analyser table

The eleven analyser crystals or segments must follow the motion of the sagittal circle as described earlier. This can be achieved by two translations (*e.g.* along Y and Z) and two rotations (*e.g.* θ and χ with rotation axes in and perpendicular to the Rowland circle). In previous multi-analyser spectrometers this was achieved by piling-up multi-stages with each crystal (Moretti Sala *et al.*, 2018). This solution was rejected for the present design because of space constraints and costs. The acceptable angular error of $<$10 μrad in the meridional direction over the scan range is furthermore beyond the achievable mechanical specifications of the components as the angular errors for each of the four components accumulate.

We conceived a new design for the displacement of the crystal analysers that minimises the angular errors and is, at the same time, less expensive than the above described four-axes solution. All crystal analysers are mounted on a custom-design cradle as shown in Figure 7A. The cradle translates along Y (TY) and rotates by θ_B around an axis that passes through the centre of the central analyser. The other ten analyser crystals are mounted left and right of the central crystal on a chained mechanical system (bronze pieces shown in Figure 7B), which is kept in contact with an underlying plate via three points that are held in place by magnets. The chained mechanics is actioned by two linear actuators via a ball-bearing accordion-like system. We call this mechanical system a "pantograph" as it resembles the pantograph toy.

Figure 7: Components of the analyser table (A): pantograph (B) and analyser module (C). *cf.* main text.

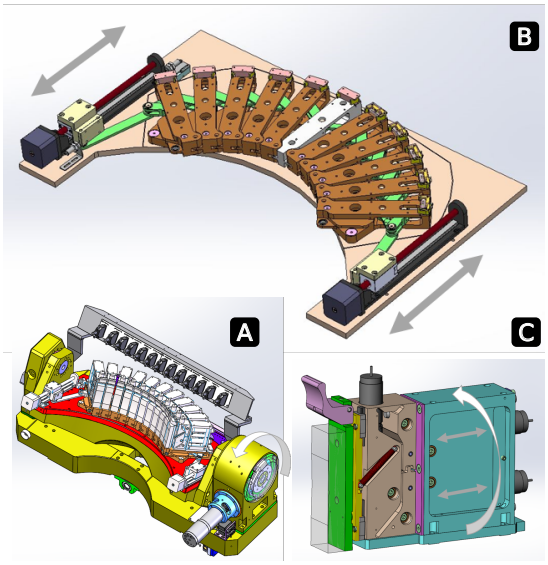

The underlying plate is made out of carbon steel (magnetic). It is rectified, polished and hardened via a surface nitridation process, ensuring minimal angular errors during the motion of the pantograph and resistance at friction with bronze. The measured flatness is below 6 μm peak-to-valley over the whole surface of 0.15 m^2. The plate is parallel to the sagittal plane and thus ensures correct positioning of all crystals. This friction design mechanics allows obtaining the required dynamical sagittal focusing for all analysers with only two motors. We note that an important property of this solution is that it can be readily adapted to a larger number of crystals and different bending radii.

The pantograph and the Bragg cradle provide combined movements for the Rowland tracking (energy scan). Additional degrees of freedom are implemented per analyser via a three axis motorised module, as shown in Figure 7C. The module carrying the analyser allows to fine tune the alignment of each analyser with respect to the central one, taken as reference. It compensates the defects introduced during the analysers productions and the inevitable misalignments of the mechanics in the whole scanning range. The motorised axis are driven by three compact high-precision linear actuators, the ESRF fixed-head micro-jacks: 1) vertical

adjustment of $\pm$2 mm stroke, 2+3) horizontal adjustment of $\pm$5 mm and θ adjustment. The last two axes are obtained by driving the actuators either in the same or the opposite directions. We chose to have three motorised degrees of freedom for each analyser for commissioning and validation of the concept. A simplified design would only require one angular adjustment in the meridional plane.

Each analyser module with its motorised degrees of freedom is mounted on the pantograph with an additional degree of freedom that allows the angular fine alignment in the sagittal direction. This alignment is performed manually with a laser (*cf.* Section 4.2). The crystal analysers are mounted (via wax or glue) on a quick release and precise mount, hold in place by magnets and with three points of contact.

3.2. Multi-wire gas detector

The second core component of the spectrometer is the detector. The first step in defining the required specifications was to simulate, via ray tracing, the focal image for the eleven cylindrical Johansson analysers. The detector is centred on the YZ plane facing the centre of the analyser table. The configuration with R = 500 mm and at $\theta_B = 35^\circ$ is shown in Figure 8A. This is the configuration where the focus spreads the most. The focal image has a butterfly-like shape because each analyser contributes with a line focus 50 mm long (twice the size of the flat side) and approximately 0.1 mm thick (vertical size of the source). The focal image of the central analyser is a horizontal line while the focal images of the side analysers are tilted. The tilting angle depends on the χ angle. For the highest tilt configuration (*cf.* Figure 8A) the total height of the combined focal image is approximately 40 mm. Furthermore, as expected from Figure 3 and shown in Figure 8A, the focal image has an energy dispersion in the horizontal direction, starting from the centre. This implies that a detector with spatial resolution along the horizontal direction will permit an in-focus energy correction. The ray tracing simulations with a source size of 0.1×0.5 mm^2 show that the energy spread along the horizontal direction

Figure 8: Multi-wire gas detector (*cf.* main text). Ray tracing simulation (A) of the focal image from the eleven analysers at 500 mm bending radius and 35° Bragg angle. Inverse vacuum chamber (B). Main components (C) of the detector: entrance x-ray window (1); gas chamber with sixteen wires (2); charge-sensitive pre-amplifier (3); baseline restore amplifier (4); Gaussian shaper (5); single channel analyser board (6); gas and cooling pipes (7). Spectral response (energy distribution) as a function of the applied potential (D) for a P Kα_1 emission line.

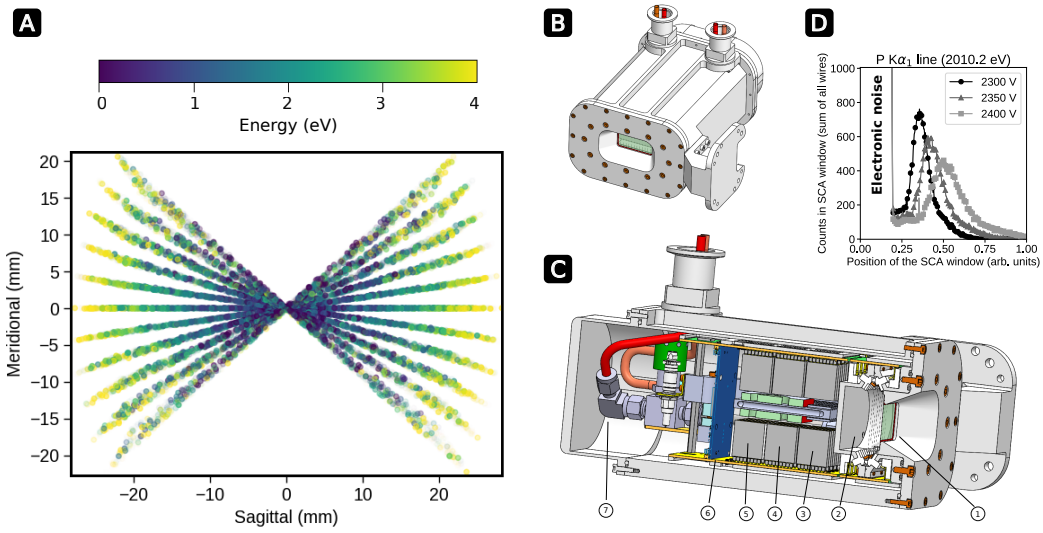

significantly evolves within a 5 mm range, not at shorter scale, thus a coarse spatial sampling is sufficient.

Consequently, from the analysis of the simulated focal images, the main specifications required for the detector are the following: 1) active area of 50 $\times$ 40 mm^2; 2) optimised photon energy range from 1.5 to 5.5 keV; 3) overall quantum efficiency (sensor absorption and electronic threshold) $\geq$80% over the whole energy range; 4) electronic noise (without x-rays) $\leq$1 event in 10 s over the whole area at minimum photon energy discriminator's threshold. 5) non-linearity $\leq$10% at 1 MHz counting rate over the whole area; 6) continuous data read-out with $\leq$20 ms delay; 7) vacuum compatibility. The detector must be mounted on moving stages covering almost 1 m^2 area. We thus required the overall weight to not exceed 8 kg.

According to these specifications, we conducted a survey study during the design phase among available commercial solutions. The conclusion was that the detector fulfilling all spec-

ifications was not available "out of the shelf" at that time or within our budget (*cf.* supplementary Section S1). For these reasons, we designed and built a multi-wire gas flow proportional counter at the ESRF. The reader interested in more details about gas detectors may refer to the book by Knoll (Knoll, 2000) or the didactic work of Winkler at al. (Winkler *et al.*, 2015). Proportional counters are frequently used in the detection and spectroscopy of low-energy x-ray radiation. This is because of their low noise and an energy resolution below 20% of the measured energy. Historically, flow proportional counters were mounted in wavelength-dispersive spectrometers for micro-analysis at electron microscopy stations (*e.g.* (Wuhrer & Moran, 2018) for a recent overview).

We developed the sixteen-wires flow proportional counter shown in Figure 8B-C. The wires are gold-coated tungsten of 50 μm diameter and mounted vertically (along the meridional direction, Y) with a horizontal spacing (along the sagittal direction, X) of 4 mm. The choice of a multi-wire configuration has two advantages: 1) increase the detector linearity; 2) obtain spatial resolution in the sagittal direction. A 90% linearity per wire of is expected at approximately 10 kHz (counts/s). The sixteen wires enable then an overall linearity up to MHz count-rates as the cylindrical crystals distribute the intensity homogeneously in the sagittal direction. The spatial sampling of the horizontal direction gives access to the energy-dispersion correction within the focal image, improving the energy resolution of the instrument. Furthermore, it allows controlling the spectrometer alignment. If fact, in case of mis-alignment not all line focii will cross the central wires, showing a signal drifting to the side wires. The data analysis presented in Section 4.3 make use of such information. The naming convention used for the commissioning and the distribution of the wires within the geometry of the spectrometer is given as supplementary Figure S1.

The gas chamber plus the electronics are encased in an "inverse vacuum" chamber, where the vacuum is outside and the atmospheric pressure inside. The chamber is mounted on the detector arm, consisting of one rotation and two translation stages. This allows positioning

the detector on all required points in the Rowland tracking space, as shown in supplementary Figure S2 while always facing the central analyser crystal. The detector chamber is connected to the outside of the vacuum vessel via two highly flexible, annular corrugated metallic hoses (Witzenmann GmbH, model RS 321). The choice of these specific hoses was made after building a dedicated prototype for measuring the forces acting on the detector during the movement (supplementary Figure S3). The hoses permit carrying the gas and cooling pipes plus the power, Ethernet and signal cables. The dimensions of the gas chamber are 113 $\times$ 50 $\times$ 40 mm^3, (width $\times$ height $\times$ thickness). It is filled with the standard P-10 gas mixture composed of 10% methane (CH_4) in Argon (Ar). The 40 mm path results in an efficiency of $\geq$90% decreasing to 60% before the Ar K-edge (3205.9 eV) (supplementary Figure S4). An x-ray window separates the gas chamber from the spectrometer vacuum. The window (MOXTEK ProLINE 20) is composed of an ultra-thin polymer of 0.6 μm thickness coated with 45 nm of Al and deposited on a metal support grid. It can hold 1.2 atm differential pressure sustaining hundreds of cycles and has an x-ray transmission $>$90% above 1 keV.

The wires are connected directly to an application-specific integrated circuit (ASIC) composed of a primary analogical stage and a secondary digital part based on a field-programmable gate array (FPGA). The analogical electronics implements a RC reset scheme of 100 μs damping time. The signal is amplified with a charge sensitive pre-amplifier, then transformed to Gaussian pulse via a shaper amplifier of 500 ns and baseline restore. The ASIC allocates commercially available amplifiers that can be easily replaced in case of failure or performance loss. Currently, the charge sensitive amplifiers are provided by Cremat Inc. The digital electronics implements a single channel analyser for the signal of each wire and outputs sixteen NIM-type signals transferred to the control computer via a differential line. Having the analogical signal processed close to the wires allows reducing the electronic noise. Furthermore, the whole electronics is water-cooled. All detector settings are remotely controlled via an Ethernet connection to a local embedded ARM computer (Qseven).

The spectral response of the detector and separation from the electronic noise is visible in Figure 8D, obtained by scanning the level of a small window in the single channel analyser. Already at a voltage of 2300 V the fluorescence peak of the P Kα_1 line at 2010.2 eV is well separated from the electronic noise peak. Increasing the voltage up to 2400 eV shifts the fluorescence signal peak to higher threshold values at the expense of energy resolution.

3.3. Sample environment

The vacuum vessel allocates a versatile sample environment volume of approximately 500 mm side, as shown in supplementary Figure S5. At the base of this volume, a breadboard allows mounting all required equipment. The standard configuration is composed of a four-axes goniometer, which provides X, Y, Z translations plus a rotation around the Z axis. The goniometers allow aligning the samples on the beam with micro-metric precision. A stroke of 40 mm is available on each translation axis, while the rotation could in principle perform 360° unless the sample environment constraints the motion.

A thick aluminium shielding positioned around the sample avoids the direct fluorescence reaching the detector or x-ray scattering background to reach the crystal analysers or the vacuum vessel walls. A set of photo-diodes are employed to measure the total fluorescence yield. An incoming x-ray beam monitor with horizontal and vertical slits is mounted upstream of the sample. The beam monitor is composed of a four-quadrant diode with a hole, reading the back-scattering from a thin Kapton foil ($<$8 μm thickness).

The vacuum vessel has a large door of square shape with a side of 700 mm in front of the sample area. During maintenance mode, the sample environment volume and the detector are accessible via this door. Four flanges are dedicated to: 1) load-lock system for quick sample change; 2) solid state detector for partial fluorescence yield analysis; 3) pressure gauge; 4) glass window for visual inspection.

The core components of the sample environment routinely available for users are the load

lock setup and the liquid He cryostat. Furthermore, two cells have been built on purpose for user experiments: one for studying *operando* gas sensors and a second one for *in situ* catalytic reactions. Both setups are described in detail in the supplementary Section S7.

The load lock setup is a commercial solution from FerroVac featuring a fast entry load lock with a quick access door and a CF40 single shaft sample transport rod of 750 mm linear travel. The transfer rod head is customised for inserting a multi-sample holder of 45 mm length and 30 mm height into the sample receptacle. The sample transfer chamber of ≈0.7 l volume is pumped from ambient pressure down to 10^{-5} mbar in less than a minute thanks to a combination of pre-pumping by a small primary pump and a turbo pump unit, which are connected by a three-way valve ensuring continuous operation of the system. This quick sample load is crucial to transfer frozen samples (*e.g.* frozen solutions) from a liquid nitrogen tank into the cold sample receptacle.

The standard sample holders are made of copper and designed to receive either three 13 mm pellets or eight 5 mm pellets (two rows of four) with a base plate having a locking mechanism for the sample transfer system. A cover piece screws over the samples and assures good thermal contact at the same time. Samples presenting safety risks (*e.g.* toxic, radioactive) can be sealed by inserting a thin Kapton foil in between the copper pieces.

The transfer system puts the sample holder in mechanical contact with the copper body of the sample receptacle, which is connected via a flexible copper braid to the cold head of a liquid He cryostat mounted directly on the spectrometer chamber on a CF63 flange. Thermal isolation from the goniometer is realised by a polyether ether ketone (PEEK) interface block supporting the sample receptacle. The required freedom in motion for the sample and necessary large optical access lead to thermal losses over the length of the copper braid limiting the working sample temperature to a minimum of approximately 22 K with the cold head staying at 12 K. The initial cool-down time for the cryostat is approximately three hours but after a sample transfer the base temperature is recovered within ten minutes.

4. Commissioning results

4.1. Johansson crystal analysers

The performance of the spectrometer critically depends on the quality of the Johansson crystals. At the early stage of the design phase we tested state-of-the-art commercially available crystals from Saint-Gobain crystals (France), Rigaku (United States), AlpyX (France) and compared them with those we fabricated at the ESRF. The results (*c.f.* supplementary Figure S7) for one commercial analyser show a performance that corresponds to the theoretical simulations demonstrating the feasibility of producing high quality Johansson cylindrical analysers. This validated the concept of our instrument where we rely on a point-to-point focusing geometry instead of a dispersive geometry, where the energy bandwidth less crucially depends on the quality of the crystal analyser. A full set of high quality crystal analysers was however not yet available and the results presented here are thus not representative for the best possible performance on the instrument. We report in Section 4.3 the results obtained with Si(111) and Si(220) 25×80 mm^2 cylindrical Johansson crystal analysers of 1 m bending radius, as we have produced at the ESRF.

We follow two manufacturing approaches in the production of cylindrical Johansson analysers: single machining and double machining. A schematic view is reported as supplementary Figure S8. The single machining consists in bending the crystal wafer on a cylindrical substrate of radius 2R and successively grind the surface to a radius R. This approach is relatively simple and results in an analyser thicker at the borders than at the centre, thus requiring bending a thick crystal. The second approach consists in a double-side grinding of a crystal to a thin meniscus (150–250 μm) of radius 2R and then bend it on a substrate of radius R. This is a time-consuming procedure that results in a uniformly thin crystal. The double machining is the approach of choice for reaching R$\leq$500 mm, as for the single machining it would result impossible to bend a crystal in the order of few mm, unless employing plastic deformation methods.

Figure 9: Johansson cylindrical crystal analysers of 25×80 mm^2 size and 1 m bending radius as produced at the ESRF: single machining (top) and double machining (bottom).

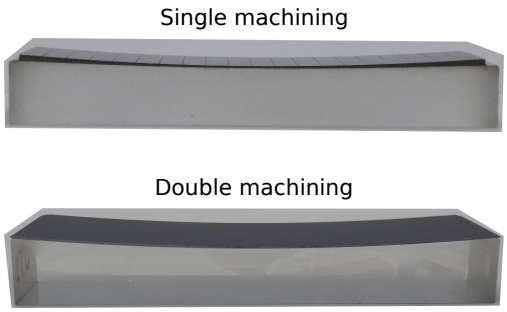

Figure 9 shows the two type of analysers we produced at the ESRF. For the single machining ones, the starting wafer has a thickness of 1.2 mm and is cut in stripes of 5 mm along the short side, with a groove of 1 mm height (incomplete cuts). The Si wafer is successively bent on a borosilicate glass substrate via a well tested anodic bonding procedure (Rovezzi *et al.*, 2017). The grooves allow to release part of the strain, resulting in a high quality bending with the substrate. In fact, in the absence of the grooves the underlying substrate cracks after the anoding bonding process. The grinding removes 0.8 mm at the centre of the analyser. This is performed with a silicon carbide powder from 17 μm down to 1 μm size. The strain and damages introduced by the grinding are released via etching in a solution of nitric and hydrofluoric acic (20:1) for 40 minutes. At the end, the surface is polished employing a 1 μm diamond powder. For the double machining, the process starts with a thick 3 mm Si wafer. First the convex face is prepared with a grinding plus polishing procedure, as previously described. Successively, this face is bonded via anodic bonding to the glass substrate. The concave face is then grounded down to a meniscus of 250 μm thickness. The final step is then an etching plus polishing.

A parameter that is found crucial in the final performances of the instrument is the optimisation of the bending radius (R). The procedure we have followed is to measure, for each analyser, the emission line of a given element at changing R in the spectrometer Rowland

tracking settings. Via the peak fitting of the signal for each independent wire, the width and height of the lines are extracted, as a function of R. The best R is then found at the minimum of a quadratic fit. An example of this procedure applied on Sulphur K$\alpha_{1,2}$ lines is reported as supplementary Figure S11. We have found that the single machining analysers have a best R matching the underlying glass substrate, that is, 1 m. In the double machining analysers R is greater than 1020 mm, beyond the scanning range of the spectrometer. How this affects the final performances of the spectrometer is discussed in the following sections. It is worth noting here that the R variance among analysers is $\pm$5 mm, bigger than the expected $\pm$2 mm, which is implemented on each analyser module.

4.2. Initial spectrometer alignment

The first step in the alignment of the spectrometer consists in a mechanical alignment with a precision of $\leq$100 μm for the absolute position of all parts. This is performed once at the installation using a laser tracker, which gives an absolute precision in space (X, Y and Z) of 10 μm at the best. The translation stages that move the entire spectrometer along Y and Z allow bringing the incoming x-ray beam into the source volume of the spectrometer. The alignment of the beam footprint on the sample along X is important to achieve the best performance and is assured by carefully considering the dimensions of the sample mount and sample thickness. We plan for a future upgrade to align the sample surface along X by an in-line optical system where the focus coincides with the spectrometer source volume.

The θ rotation (TR) and all crystal analyser mounts (athN) are calibrated at 90° with an inclinometer with a precision below 5 μrad. The centre of the detector window is positioned on the Rowland circle by introducing an offset in the control system representing the origin of the two inclined translation axes defining the trajectory space (DY, DZ). The χ angles for each crystal are aligned using a laser. This is performed only once, when mounting the analysers modules on the pantograph.

The final alignment is performed with x-rays. Once a strong fluorescence line is excited, the spectrometer is driven to the nominal emission energy and then each athN is aligned at the maximum intensity. It is found that this is the only fine alignment that needs to be performed for each fluorescence line or group of lines. We have not found any benefit in fine tuning the vertical correction for each analyser. We note that the bending radius of the crystal analysers is not necessarily the one given by the substrate radius. It is thus important to find the actual bending radius, as previously discussed. Currently, the spectrometer motion assumes identical bending radii for all crystals.

4.3. Instrumental energy resolution

The figure of merit of the spectrometer performance is the energy broadening as function of the Bragg angle. This is extracted with the following procedure. First, we measure an emission spectrum, composed of a single or multiple lines. The spectrum is fitted with Voigt profiles, that is, a convolution of Gaussian and Lorentzian profiles, accounting respectively for the instrumental and intrinsic broadening. The instrumental/Gaussian width, w_G, is taken from the full-width-at-half-maximum (FWHM) of the Voigt profile, w_V, using the modified Whiting relation (Olivero & Longbothum, 1977): $w_V \approx 0.5346 w_L + \sqrt{0.2169 w_L^2 + w_G^2}$, where the intrinsic/Lorentzian width, w_L, is kept fixed at the tabulated value. Furthermore, if the measured emission spectrum contains two lines (*e.g.* K$\alpha_{1,2}$, L$\alpha_{1,2}$), the energy separation and peak ratio of the two lines are kept fixed at tabulated values, not fitted. The peak-fitting is performed with the Lmfit code (Newville *et al.*, 2019) and the signal of each wire is taken separately. Further details of the fitting procedure are reported in supplementary Section S11.

The results of the fits are shown in Figure 10 and reported in Table 1. A series of emission lines from K, L and M edges were measured, both with Si(111) and Si(220) crystal analysers, sampling the entire angular range. The averaged data are shown in supplmentary Figure S9. Metallic foils were used as samples, if available. Otherwise, the emission lines from other

Figure 10: Spectrometer resolution function de-convoluted from the measured emission lines and compared with the expected performances simulated via ray tracing (*cf.* main text).

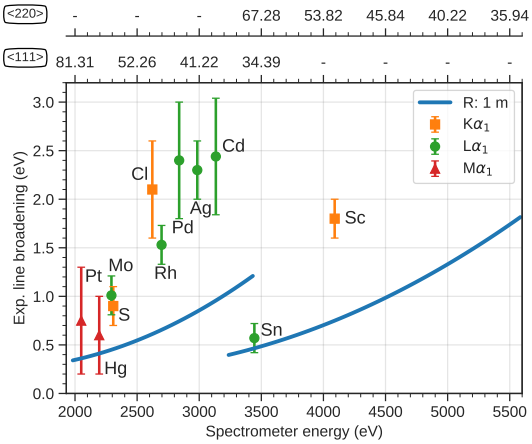

compounds (*e.g.* oxides) were used for a given element. The broadening reported here may be larger than the real instrumental broadening of the spectrometer because lines splittings (*e.g.* multiplets) are not considered in the analysis. The assumption made in the peak fitting is that the Lorentzian component is fixed to the tabulated values. The error bars reported in Figure 10 are obtained from the standard deviation of the results taken individually from each wire signal and analyser crystal mounted on the eleven available stages.

The experimental line broadening is found to range between 0.5 eV and 2.5 eV as the Bragg angle reduces. We compare these results with the expected performances as simulated with ray tracing (*cf.* Section 2). The increasing broadening with lower Bragg angle behaves as expected. The measured energy bandwidth is compatible with the simulations down to a Bragg angle of 70°, while diverges from the theoretical curves at lower angles reaching approximately twice the theoretical values at 35°. This is due to the poor quality of the single machining Johansson analysers. In fact, we tested two Si(111) analysers produced via double machining, one from a commercial provider (SG) and a second one from us (ESRF), in the same experimental set-up at high energy. The Cu K$\alpha_{1,2}$ lines were measured with the Si(444) and Si(333) reflections at Bragg angles of 79.309° and 47.475° (*cf.* Table 1). The experimental energy broadening at high energy for the commercial analyser follows the the-

Table 1: Peak-fitting results for a series of emission lines covering the whole Bragg angular range (θ_{B}), partially shown in Figure 10. The analysers without a label are produced via single machining, while those produced via double machining are labelled by the provider: commercial (SG) or ESRF. Last two columns report, respectively, the intrinsic FWHM of the line and the experimental one. The error bar on the last digit is reported in parenthesis.

El.	Line	Energy (eV)	Analyser Mat(*hkl*)	θ_{B} (°)	Sample	$\mathrm{FWHM_{th}}$ (eV)	$\mathrm{FWHM_{exp}}$ (eV)
Pt	Mα_1	2050.0	Si(111)	74.667	$\mathrm{Pt_{foil}}$	2.39	0.75(55)
Hg	Mα_1	2195.0	Si(111)	64.250	HgSe	2.59	0.6(4)
Mo	Lα_1	2293.2	Si(111)	59.550	$\mathrm{Mo_{foil}}$	1.81	1.0(2)
S	Kα_1	2307.8	Si(111)	58.945	$\mathrm{ZnSO_4}$	0.61	0.9(2)
S	Kα_1	2307.8	$\mathrm{Si(111)_{SG}}$	58.945	ZnS	0.61	0.7(1)
Cl	Kα_1	2622.4	Si(111)	48.929	KCl	0.68	2.1(5)
Rh	Lα_1	2696.8	Si(111)	47.147	$\mathrm{Rh_{metal}}$	2.17	1.7(2)
Pd	Lα_1	2838.6	Si(111)	44.145	$\mathrm{Pd_{foil}}$	2.31	2.4(6)
Ag	Lα_1	2984.4	Si(111)	41.487	$\mathrm{Ag_{foil}}$	2.45	2.3(3)
Cd	Lα_1	3133.8	Si(111)	39.114	$\mathrm{Cd_{foil}}$	2.58	2.4(6)
Sn	Lα_1	3444.0	Si(111)	35.033	$\mathrm{Sn_{metal}}$	2.87	3.6(6)
Sn	Lα_1	3444.0	Si(220)	69.622	$\mathrm{Sn_{metal}}$	2.87	0.6(2)
Sn	Lβ_3	3750.3	Si(220)	59.413	$\mathrm{Sn_{metal}}$	5.70	1.9(6)
Sc	Kα_1	4090.6	Si(220)	52.115	$\mathrm{Sc_2O_3}$	1.06	1.8(2)
Cu	Kα_1	8047.8	$\mathrm{Si(444)_{SG}}$	79.309	$\mathrm{Cu_{foil}}$	2.10	0.96(40)
Cu	Kα_1	8047.8	$\mathrm{Si(444)_{ESRF}}$	79.309	$\mathrm{Cu_{foil}}$	2.10	1.3(2)
Cu	Kα_1	8047.8	$\mathrm{Si(333)_{SG}}$	47.475	$\mathrm{Cu_{foil}}$	2.10	1.83(40)
Cu	Kα_1	8047.8	$\mathrm{Si(333)_{ESRF}}$	47.475	$\mathrm{Cu_{foil}}$	2.10	3.3(3)

oretical performance, while the one produced at ESRF has still a lower performance at low angles. The reason of this discrepancy has been found related to a wrong radius of the crystal planes, out of the spectrometer range. Unfortunately, the excellent performances obtained by the commercial analyser at high energy are not confirmed when measuring at low energy, as is the case here for S (*cf.* $\mathrm{Si(111)_{SG}}$ in Table 1). The energy bandwidth is still at 0.7(1) eV, not reaching the expected performance below 0.5 eV. This means that the quality of the analyser surface should be improved. Based on these results, we have planned a newer production series of double machining analysers that should fix both issues.

4.4. First results for HERFD-XANES

The point-to-point focusing geometry was chosen because an important application of the instrument is to record HERFD-XANES. An example at the L_3 and L_1 edges of Tin (Sn) is shown in Figure 11. The experimental energy broadening with the Si(220) crystals is 0.6(2) eV at Lα_1 (L_3-M_5) and 1.9(6) eV at Lβ_3 (L_1-M_3). The natural bandwidth of those lines is 2.87 eV (Lα_1) and 5.7 eV (Lβ_3). This introduces a sharpening effect on the XANES features that is clearly visible when compared to the total fluorescence yield (TFY) measurements (Figure 11A,B). The additional spectral features that become visible provide important information when comparing the experimental data to quantum chemical simulations.

The high energy resolution in the fluorescence detection in HERFD-XANES as compared to conventional XANES effectively suppresses the background arising from fluorescence of other elements in the sample with absorption edges at lower energies (Merkulova *et al.*, 2019). Another case where this is helpful is when the L_1 edge is to be measured without being affected by the background arising from L_3 and L_2 edges at lower energy. As an example, metallic Sn has the electronic configuration of $4d^{10}5s^25p^2$ and the highest oxidation state is 4^+. This means that the $4d$ shell is always filled and measuring at the L_3 edge (transitions to d-orbitals) does not give direct information on the Sn valence shells to determine, *e.g.*, the oxidation state, as it is difficult to correlate the edge shift to the oxidation state. This is visible in Figure 11C. In this case, measuring at L_1 edge is advantageous, as the transition is to empty and not localised $5p$ states. Thus the edge clearly shifts with oxidation state (Figure 11D).

5. Conclusions

We have presented the design and performances of a tender x-ray emission spectrometer based on an array of eleven cylindrically bent Johansson crystal analysers in point-to-point scanning geometry. This design ensures that the entire available solid angle (up to 87 msr) is used within the energy bandwidth of the instrument and thus achieving high detection efficiency

Figure 11: Example of collected data on Sn at L3 and L1 edges: (A, B) sharpening effect for SnO_2; (C, D) spectra for three nominal oxidation states.

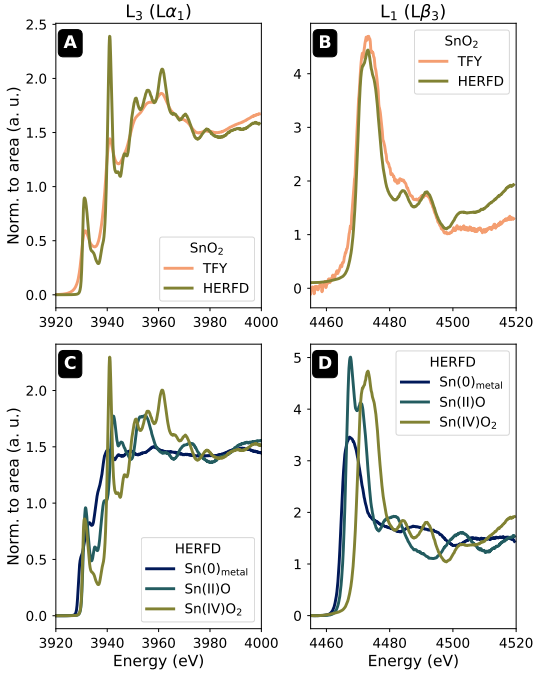

for HERFD-XANES. An innovative design for the crystal analysers table allows driving the sagittal focusing dynamically with only two actuators. This design can be adapted to a larger number of analyser crystals and different bending radii. A series of emission lines in the tender x-ray energy range was measured to evaluate the performance of the instrument that is currently limited by the quality of the single machining Johansson analyser crystals. The performance will improve considerably with the installation of double-machining crystals.

6. Acknowledgements

We are indebted to the instrumentation services, administration, directorate and technical infrastructure divisions of the ESRF for help during the design, procurement and installation phases of the project. M. R. is grateful to Jean-Louis Hazemann and the FAME group for a wonderful support during the commissioning of the instrument, data analysis and writing of the manuscript. This work was financially supported by the French National Research Agency

(ANR) under Grant ANR-10-EQPX-27-01 (EcoX Equipex).

References

Abraham, B., Nowak, S., Weninger, C., Armenta, R., Defever, J., Day, D., Carini, G., Nakahara, K., Gallo, A., Nelson, S., Nordlund, D., Kroll, T., Hunter, M. S., van Driel, T., Zhu, D., Weng, T.-C., Alonso-Mori, R. & Sokaras, D. (2019). *Journal of Synchrotron Radiation*, **26**(3), 629–634.
URL: *http://scripts.iucr.org/cgi-bin/paper?S1600577519002431*

Alonso Mori, R., Paris, E., Giuli, G., Eeckhout, S. G., Kavcic, M., Zitnik, M., Bucar, K., Pettersson, L. G. M. & Glatzel, P. (2009). *Analytical Chemistry*, **81**(15), 6516–6525.
URL: *http://pubs.acs.org/doi/abs/10.1021/ac900970z*

Bauer, M. (2014). *Phys. Chem. Chem. Phys.* **16**(27), 13827–13837.
URL: *http://xlink.rsc.org/?DOI=C4CP00904E*

DeBeer, S. & Bergmann, U. (2016). In *Encyclopedia of Inorganic and Bioinorganic Chemistry*, pp. 1–14. Chichester, UK: John Wiley & Sons, Ltd.
URL: *http://doi.wiley.com/10.1002/9781119951438.eibc2158*

Doriese, W. B., Abbamonte, P., Alpert, B. K., Bennett, D. A., Denison, E. V., Fang, Y., Fischer, D. A., Fitzgerald, C. P., Fowler, J. W., Gard, J. D., Hays-Wehle, J. P., Hilton, G. C., Jaye, C., McChesney, J. L., Miaja-Avila, L., Morgan, K. M., Joe, Y. I., O'Neil, G. C., Reintsema, C. D., Rodolakis, F., Schmidt, D. R., Tatsuno, H., Uhlig, J., Vale, L. R., Ullom, J. N. & Swetz, D. S. (2017). *Review of Scientific Instruments*, **88**(5), 053108.
URL: *http://aip.scitation.org/doi/10.1063/1.4983316*

Dousse, J.- & Hoszowska, J. (2014). In *High-Resolution XAS/XES*, chap. 2, pp. 27–58. CRC Press.
URL: *http://www.crcnetbase.com/doi/abs/10.1201/b17184-3*

Glatzel, P. & Bergmann, U. (2005). *Coordination Chemistry Reviews*, **249**(1-2), 65–95.
URL: *http://linkinghub.elsevier.com/retrieve/pii/ S0010854504001146*

Guijarro, M. & others (2018). In *Proc. of International Conference on Accelerator and Large Experimental Control Systems (ICALEPCS'17), Barcelona, Spain, 8-13 October 2017*, no. 16 in International Conference on Accelerator and Large Experimental Control Systems, pp. 1060–1066. Geneva, Switzerland: JACoW.
URL: *http://jacow.org/icalepcs2017/papers/webpl05.pdf*

Hayashi, H. (2000). In *Encyclopedia of Analytical Chemistry*, pp. 1–31. Chichester, UK: John Wiley & Sons, Ltd.
URL: *http://onlinelibrary.wiley.com/doi/10.1002/ 9780470027318.a9389/full http://doi.wiley.com/10.1002/ 9780470027318.a9389*

Holden, W. M., Hoidn, O. R., Ditter, A. S., Seidler, G. T., Kas, J., Stein, J. L., Cossairt, B. M., Kozimor, S. A., Guo, J., Ye, Y., Marcus, M. A. & Fakra, S. (2017). *Review of Scientific Instruments*, **88**(7), 073904.
URL: *http://arxiv.org/abs/1704.07496 http://dx.doi.org/10.1063/ 1.4994739 http://aip.scitation.org/doi/10.1063/1.4994739*

Hoszowska, J., Dousse, J.-C., Kern, J. & Rhême, C. (1996). *Nuclear Instruments and Methods in Physics Research Section A: Accelerators, Spectrometers, Detectors and Associated Equipment*, **376**(1), 129–138.
URL: *http://linkinghub.elsevier.com/retrieve/pii/ 0168900296002628*

Huotari, S., Albergamo, F., Vanko, G., Verbeni, R. & Monaco, G. (2006). *Review of Scientific Instruments*, **77**(5), 053102.
URL: *http://scitation.aip.org/content/aip/journal/rsi/77/5/ 10.1063/1.2198805*

Johansson, T. (1933). *Zeitschrift fuer Physik*, **82**(7-8), 507–528.
URL: *http://www.springerlink.com/index/10.1007/BF01342254 http://link.springer.com/10.1007/BF01342254*

Kavčič, M., Bučar, K., Petric, M., Žitnik, M., Arčon, I., Dominko, R. & Vizintin, A. (2016). *The Journal of Physical Chemistry C*, **120**(43), 24568–24576.
URL: *http://pubs.acs.org/doi/abs/10.1021/acs.jpcc.6b06705 http://pubs.acs.org/doi/10.1021/acs.jpcc.6b06705*

Kavčič, M., Budnar, M., Mühleisen, A., Gasser, F., Žitnik, M., Bučar, K. & Bohinc, R. (2012). *The Review of scientific instruments*, **83**(3), 033113.
URL: *http://www.ncbi.nlm.nih.gov/pubmed/22462912*

Knoll, G. F. (2000). *Radiation Detection and Measurement*. 3rd ed.

Kvashnina, K. O., Butorin, S. M., Martin, P. & Glatzel, P. (2013). *Physical Review Letters*, **111**(25), 253002.
URL: *https://link.aps.org/doi/10.1103/PhysRevLett.111.253002*

Kvashnina, K. O., Romanchuk, A. Y., Pidchenko, I., Amidani, L., Gerber, E., Trigub, A., Rossberg, A., Weiss, S., Popa, K., Walter, O., Caciuffo, R., Scheinost, A. C., Butorin, S. M. & Kalmykov, S. N. (2019). *Angewandte Chemie International Edition*.
URL: *http://doi.wiley.com/10.1002/anie.201911637*

Meisel, A., Leonhardt, G. & Szargan, R. (1989). *X-Ray Spectra and Chemical Binding*. Springer-Verlag Berlin Heidelberg.
URL: *https://www.springer.com/gp/book/9783642822643*

Merkulova, M., Mathon, O., Glatzel, P., Rovezzi, M., Batanova, V., Marion, P., Boiron, M.-C. & Manceau, A. (2019). *ACS Earth and Space Chemistry*, **3**(9), 1905–1914.
URL: *http://pubs.acs.org/doi/10.1021/acsearthspacechem.9b00099*

Moretti Sala, M., Martel, K., Henriquet, C., Al Zein, A., Simonelli, L., Sahle, C. J., Gonzalez, H., Lagier, M.-C., Ponchut, C., Huotari, S., Verbeni, R., Krisch, M. & Monaco, G. (2018). *Journal of Synchrotron Radiation*, **25**(2), 580–591.
URL: *http://scripts.iucr.org/cgi-bin/paper?S1600577518001200*

Mori, R. A., Paris, E., Giuli, G., Eeckhout, S. G., Kavcic, M., Zitnik, M., Bucar, K., Pettersson, L. G. M. & Glatzel, P. (2010). *Inorganic Chemistry*, **49**(14), 6468–6473.
URL: *http://pubs.acs.org/doi/abs/10.1021/ic100304z*

Newville, M., Otten, R., Nelson, A., Ingargiola, A., Stensitzki, T., Allan, D., Fox, A., Carter, F., Michał, Pustakhod, D., Ram, Y., Glenn, Deil, C., Stuermer, Beelen, A., Frost, O., Zobrist, N., Pasquevich, G., Hansen, A. L. R., Stark, A., Spillane, T., Caldwell, S., Polloreno, A., andrewhannum, Borreguero, J., Fraine, J., deep-42-thought, Maier, B. F., Gamari, B. & Almarza, A., (2019). lmfit/lmfit-py 0.9.14.
URL: *https://zenodo.org/record/3381550*

Olivero, J. & Longbothum, R. (1977). *Journal of Quantitative Spectroscopy and Radiative Transfer*, **17**(2), 233–236.
URL: *http://linkinghub.elsevier.com/retrieve/pii/0022407377901613 https://linkinghub.elsevier.com/retrieve/pii/0022407377901613*

Proux, O., Lahera, E., Del Net, W., Kieffer, I., Rovezzi, M., Testemale, D., Irar, M., Thomas, S., Aguilar-Tapia, A., Bazarkina, E. F., Prat, A., Tella, M., Auffan, M., Rose, J. & Hazemann, J.-l. (2017). *Journal of Environment Quality*, **46**(6), 1146.
URL: *https://dl.sciencesocieties.org/publications/jeq/abstracts/0/0/jeq2017.01.0023 https://dl.sciencesocieties.org/publications/jeq/abstracts/46/6/1146*

Sanchez del Rio, M., Canestrari, N., Jiang, F. & Cerrina, F. (2011). *Journal of Synchrotron Radiation*, **18**(5), 708–716.
URL: *http://scripts.iucr.org/cgi-bin/paper?S0909049511026306 http://www.pubmedcentral.nih.gov/articlerender.fcgi?artid=3267628tool=pmcentrez rendertype=abstract*

Sanchez del Rio, M., Perez-Bocanegra, N., Shi, X., Honkimäki, V. & Zhang, L. (2015). *Journal of Applied Crystallography*, **48**(2), 477–491.
URL: *http://scripts.iucr.org/cgi-bin/paper?S1600576715002782*

Rovezzi, M. (2017). *Zenodo*.
URL: *https://doi.org/10.5281/zenodo.597031*

Rovezzi, M. & Glatzel, P. (2014). *Semiconductor Science and Technology*, **29**(2), 023002.
URL: *http://stacks.iop.org/0268-1242/29/i=2/a=023002?key=crossref.801cef18c0c556e30c08b4bb6fd87e6b*

Rovezzi, M., Lapras, C., Manceau, A., Glatzel, P. & Verbeni, R. (2017). *Review of Scientific Instruments*, **88**(1), 013108.
URL: *http://arxiv.org/abs/1609.08894 http://aip.scitation.org/doi/10.1063/1.4974100*

Rowland, H. A. (1882). *Philosophical Magazine*, **13**, 477.
URL: *http://zs.thulb.uni-jena.de/receive/jportal_jpvolume_0128126*

Rueff, J. & Shukla, A. (2013). *Journal of Electron Spectroscopy and Related Phenomena*, **188**(2010), 10–16.
URL: *http://linkinghub.elsevier.com/retrieve/pii/S0368204813000790 https://linkinghub.elsevier.com/retrieve/pii/S0368204813000790*

Sa, J. (ed.) (2014). *High-Resolution XAS/XES*. CRC Press.
URL: *https://www.taylorfrancis.com/books/9781466592995*

Schoonjans, T., Brunetti, A., Golosio, B., Sanchez del Rio, M., Solé, V. A., Ferrero, C. & Vincze, L. (2011). *Spectrochimica Acta Part B: Atomic Spectroscopy*, **66**(11-12), 776–784.
URL: *http://linkinghub.elsevier.com/retrieve/pii/S0584854711001984*

Thomas, R., Kas, J., Glatzel, P., Al Samarai, M., de Groot, F. M. F., Alonso Mori, R., Kavčič, M., Zitnik, M., Bucar, K., Rehr, J. J. & Tromp, M. (2015). *The Journal of Physical Chemistry C*, p. 150126100226006.
URL: *http://pubs.acs.org/doi/abs/10.1021/jp509376q*

Thompson, P. B. J., Nguyen, B. N., Nicholls, R., Bourne, R. A., Brazier, J. B., Lovelock, K. R. J., Brown, S. D., Wermeille, D., Bikondoa, O., Lucas, C. A., Hase, T. P. A. & Newton, M. A. (2015). *Journal of Synchrotron Radiation*, **22**(6), 1426–1439.
URL: *http://scripts.iucr.org/cgi-bin/paper?S1600577515016148*

Welter, E., Machek, P., Dräger, G., Brüggmann, U. & Fröba, M. (2005). *Journal of synchrotron radiation*, **12**(Pt 4), 448–54.
URL: *http://dx.doi.org/10.1107/S0909049505007843*

Wilhelm, F., Garbarino, G., Jacobs, J., Vitoux, H., Steinmann, R., Guillou, F., Snigirev, A., Snigireva, I., Voisin, P., Braithwaite, D., Aoki, D., Brison, J.-P., Kantor, I., Lyatun, I. & Rogalev, A. (2016). *High Pressure Research*, **36**(3), 445–457.
URL: *https://www.tandfonline.com/doi/full/10.1080/ 08957959.2016.1206092*

Winkler, A., Karadzhinova, A., Hildén, T., Garcia, F., Fedi, G., Devoto, F. & Brücken, E. J. (2015). *American Journal of Physics*, **83**(8), 733–740.
URL: *http://arxiv.org/abs/1509.02379 http://dx.doi.org/10.1119/ 1.4923022 http://aapt.scitation.org/doi/10.1119/1.4923022*

Wittry, D. B. & Li, R. Y. (1993). *Review of Scientific Instruments*, **64**(8), 2195–2200.
URL: *http://link.aip.org/link/RSINAK/v64/i8/p2195/s1 Agg=doi http://aip.scitation.org/doi/10.1063/1.1143959*

Wittry, D. B. & Sun, S. (1990*a*). *Journal of Applied Physics*, **68**(2), 387–391.
URL: *http://link.aip.org/link/JAPIAU/v68/i2/p387/s1Agg=doi http: //aip.scitation.org/doi/10.1063/1.346834*

Wittry, D. B. & Sun, S. (1990*b*). *Journal of Applied Physics*, **67**(4), 1633.
URL: *http://scitation.aip.org/content/aip/journal/jap/67/4/ 10.1063/1.345629*

Wittry, D. B. & Sun, S. (1991). *Journal of Applied Physics*, **69**(7), 3886.
URL: *http://link.aip.org/link/JAPIAU/v69/i7/p3886/s1 Agg=doi http://scitation.aip.org/content/aip/journal/jap/69/ 7/10.1063/1.348446*

Wittry, D. B. & Sun, S. (1992). *Journal of Applied Physics*, **71**(2), 564–568.
URL: *http://scitation.aip.org/content/aip/journal/jap/71/2/ 10.1063/1.350406 http://aip.scitation.org/doi/10.1063/ 1.350406*

Wuhrer, R. & Moran, K. (2018). *IOP Conference Series: Materials Science and Engineering*, **304**, 012021.
URL: *http://stacks.iop.org/1757-899X/304/i=1/a=012021? key=crossref.d1c503dd4b4923c12f9c220f29603b46*

Synopsis

In-vacuum tender x-ray emission spectrometer based on an array of eleven Johansson-type crystal analysers arranged in a point-to-point Rowland circle geometry.

TEXS: in-vacuum tender x-ray emission spectrometer based on eleven Johansson crystal anlysers - SUPPORTING INFORMATION

Mauro Rovezzi,[1,2,a)] Alistair Harris,[3] Blanka Detlefs,[2] Timothy Bohdan,[2] Artem Sviazhin,[2] Alessandro Santambrogio,[2] David Degler,[2] Rafal Baran,[2] Benjamin Reynier,[2] Pedro Noguera Crespo,[4] Catherine Heyman,[3] Hans-Peter Van Der Kleij,[2] Pierre Van Vaerenbergh,[2] Philippe Marion,[2] Hugo Vitoux,[2] Christophe Lapras,[2] Roberto Verbeni,[2] Menhard Menyhert Kocsis,[2] Alain Manceau,[5] and Pieter Glatzel[2,b)]

[1)] *Univ. Grenoble Alpes, CNRS, IRD, Irstea, Météo France, OSUG, FAME, 71 avenue des Martyrs, CS 40220, 38043, Grenoble, France*

[2)] *European Synchrotron Radiation Facility, 71 avenue des Martyrs, CS 40220, 38043, Grenoble, France*

[3)] *Design et Mécanique, Les Coings, 38210, Montaud, France*

[4)] *Added Value Solutions (AVS), Pol. Ind. Sigma Xixilion Kalea 2, Bajo Pabellón 10, 20870, Elgoibar, Spain*

[5)] *ISTerre, Université Grenoble Alpes, CNRS, CS 40700, 38058, Grenoble, France*

(Dated: 2019-11-18)

Keywords: X-ray instrumentation, Wavelength dispersive spectrometer, X-ray optics, Tender x-rays, Johansson crystal analysers

[a)] Electronic mail: mauro.rovezzi@esrf.fr

[b)] Electronic mail: glatzel@esrf.fr

SI for TEXSpap version 0.2.47.1

S1. DETECTOR ALTERNATIVES TO THE PROPORTIONAL COUNTER

We examined other solutions for the detector among existing commercial alternatives or promising projects in development. The most suited detector for such an application would be a scientific-quality large area charged-coupled device (CCD). CCDs are widely used in soft x-ray RIXS spectrometers for their low electronic noise and small pixel size. Furthermore, it is possible to run them in spectroscopy mode[S1], enhancing the possibility to reduce the background level of the measured signal. Commercial sensors have a standard size of approximately 27 $\times$ 27 mm^2, that is, 2048 square pixels of 13 μm side. The drawback of such sensors is the read-out time, being as slow as 500 ms for unbind mode, well above the required 20 ms. Fast readout and large area CCDs exists, like the pnCCD[S2] or the fastCCD[S3]. These extremely high performance detectors, initially developed for astronomical applications in space telescopes, are expensive. An alternative to CCDs are silicon drift detectors (SDDs). Typical sensors are of 50 mm^2 area, thus to cover the required area of 2000 mm^2 one could opt for a multi-element array[S4] or pixelated sensors[S5]. Nevertheless, this solution is challenging. Hybrid pixel detectors, that is, a pixelated sensor (usually Si) bump-bonded to a large area CMOS have also demonstrated some applications in the low energy side[S6,S7]. Recently, direct reading of mass production CMOS cameras was shown as a possible alternative for tender x-rays[S8,S9]. The drawback of these CMOS-based detectors is their quantum efficiency, usually below 20%. In fact, either the high noise level imposes an electronic threshold that barely allows the signal to be measured (the case of hybrid pixel detectors) or the active layer of the CMOS is too thin (the case of direct CMOS reading).

S2. NAMING CONVENTION FOR WIRE SIGNALS AND ANALYSER MODULES

The naming convention for the detector wires (`gN`) and analysers modules (`athN`) is given in Figure S1. The figure permits understanding the origin of the signal detected on each wire and the arrangement of the analysers with respect to the incoming x-ray beam (X direction).

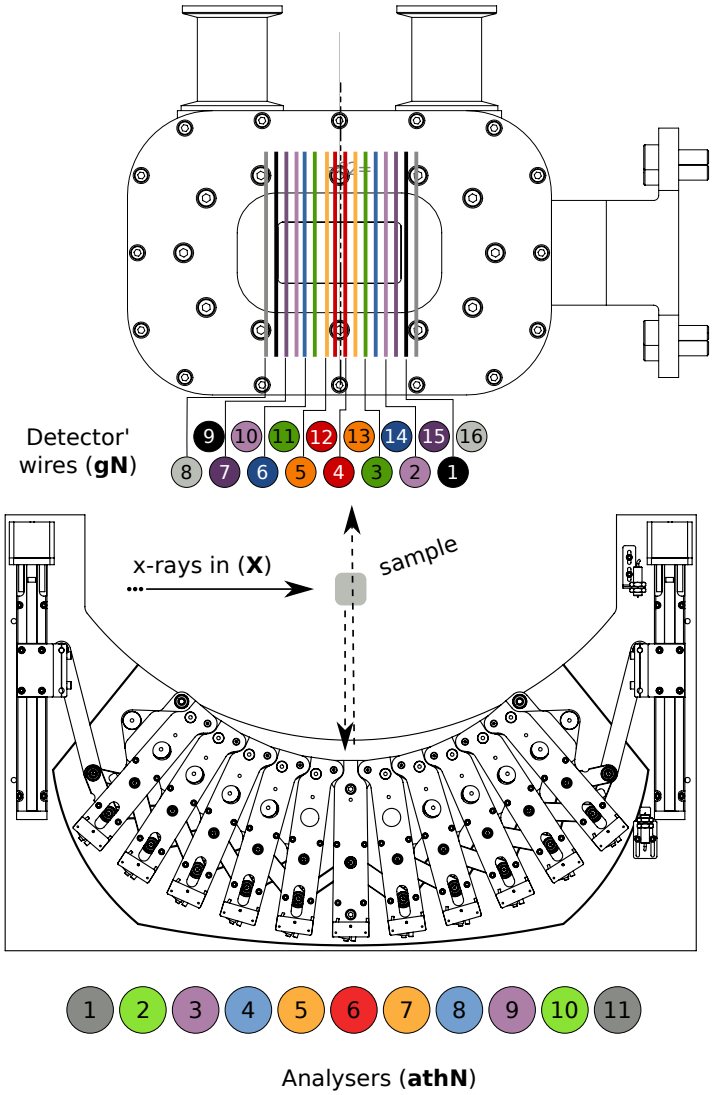

Figure S1. Naming of the detector wires signals (gN) and analyser modules (athN) used during the commissioning and data analysis. Detector and analyser table are given in a projected view such as looking from the analyser door of the spectrometer, that is, the incoming x-ray beam is coming from the left. Dimensions are not in scale. A colour coding is used to show the central symmetry.

S3. DETECTOR TRAJECTORIES AND HOSES

The trajectories for R=1020 mm and R=480, respectively, maximum and minimum allowed diameter of the Rowland circle are shown in Figure S2. The simulation of the hoses position at given angular positions is also shown. Those simulations have been used for testing the behaviour of the metallic hoses and measuring the forces on the detector's arm, as shown in Figure S3.

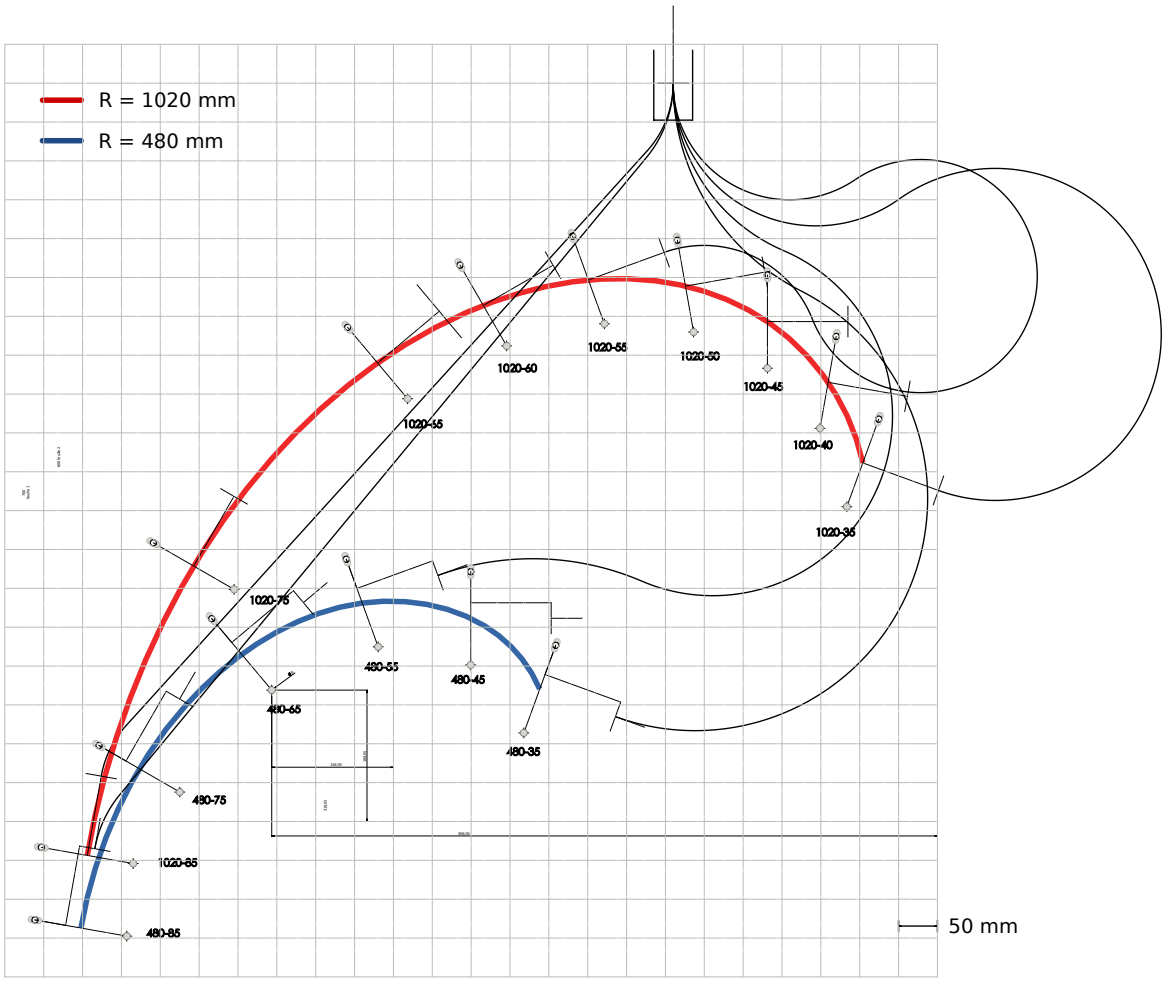

Figure S2. Trajectories of the detector's chamber with hoses for two extreme radii.

S4. GAS DETECTOR EFFICIENCY

The gas detector efficiency, that is, the x-ray absorption (in the energy range of interest) by the P-10 mixture at 1 bar and room temperature in the 4 cm path is shown in Figure S4.

S5. SAMPLE ENVIRONMENT

The sample environment space is shown in Figure S5.

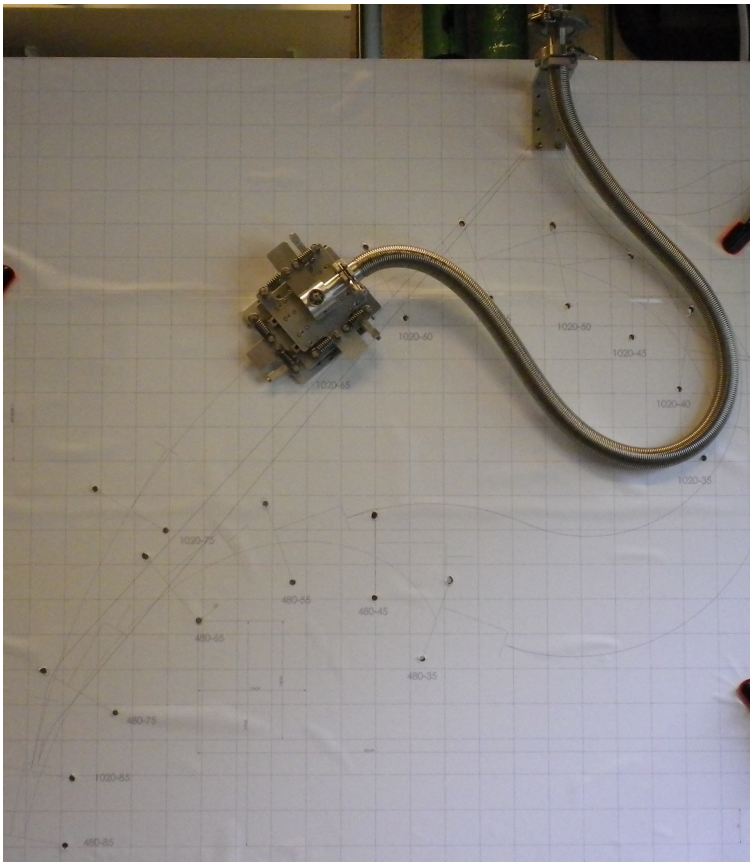

Figure S3. Prototype mechanics for testing the metallic hoses in real conditions and measuring the forces on the detector's arm.

S6. *OPERANDO* CELL FOR GAS SENSORS

In-situ and *operando* XAS are an essential method to understand synthesis-structure-function-relationships of metal oxide based gas sensing materials[S10,S11]. The elements of interest are those from base materials such as SnO_2, In_2O_3 and WO_3, and additives like Rh, Pd, Pt and Au. In case of 5*d*-elements there are various examples using HERFD-XAS to study the behaviour of additives during gas sensing[S12,S13], while in case of 4*d*-elements K-edges were studied using conventional XAS[S14–S16]. Extending the spectral range to tender X-rays allows studying the L-edges of 4*d*-elements and will provide unprecedented insights in the gas sensing process of pristine, doped and loaded metal oxide gas sensing materials.

For TEXS a suitable operando gas sensor cell (Figure S6A) was designed, which allows dynamically dosing different gas flows. The sensor socket is designed to mount research-type gas sensor substrates[S17] and is equipped with electrical connections to supply a heating voltage and continuously read the sensor response during the experiment. Successful tests were done studying

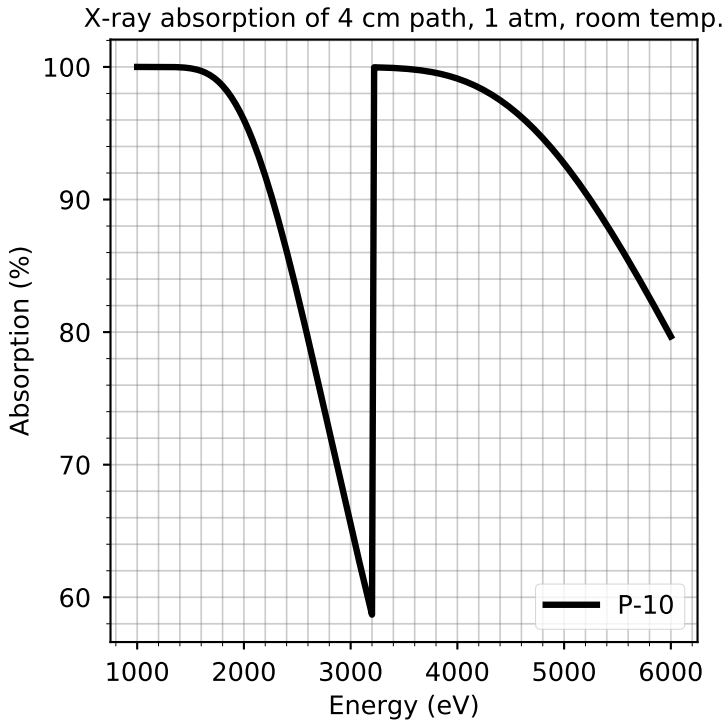

Figure S4. Gas detector efficiency in the energy range of interest.

a 2 wt% Pd-loaded SnO_2 gas sensor at 300 °C in different atmospheres (Figure S6B). The recorded HERFD-XANES spectra show a clear effect of the atmospheric composition on the Pd sites.

S7. INITIAL CHARACTERISATION OF COMMERCIAL ANALYSERS

A brief summary of the characterisation of two selected commercial Johansson crystal analysers (double machining) and one produced at the ESRF (single machining) is shown in Figure S7. The measurements were performed on the high energy spectrometer of ID26 at 6.5 keV, using Si(333) reflection at a Bragg angle of 65 °, following a well established procedure[S18]. During these measurements, a square avalanche photo diode detector of 10 mm side was used. This means that only a central area of 5 mm side along the flat direction was probed. The performance showed by the "Commercial 1" analyser corresponds to what is expected by a ray tracing simulation. The ESRF analyser corresponds to a first production series of single machining analysers, that is, without grooves. The grooves and the optimisation of the surface polishing (*cf.* main text) have permitted to remove the side tails visible in the reflectivity curve.

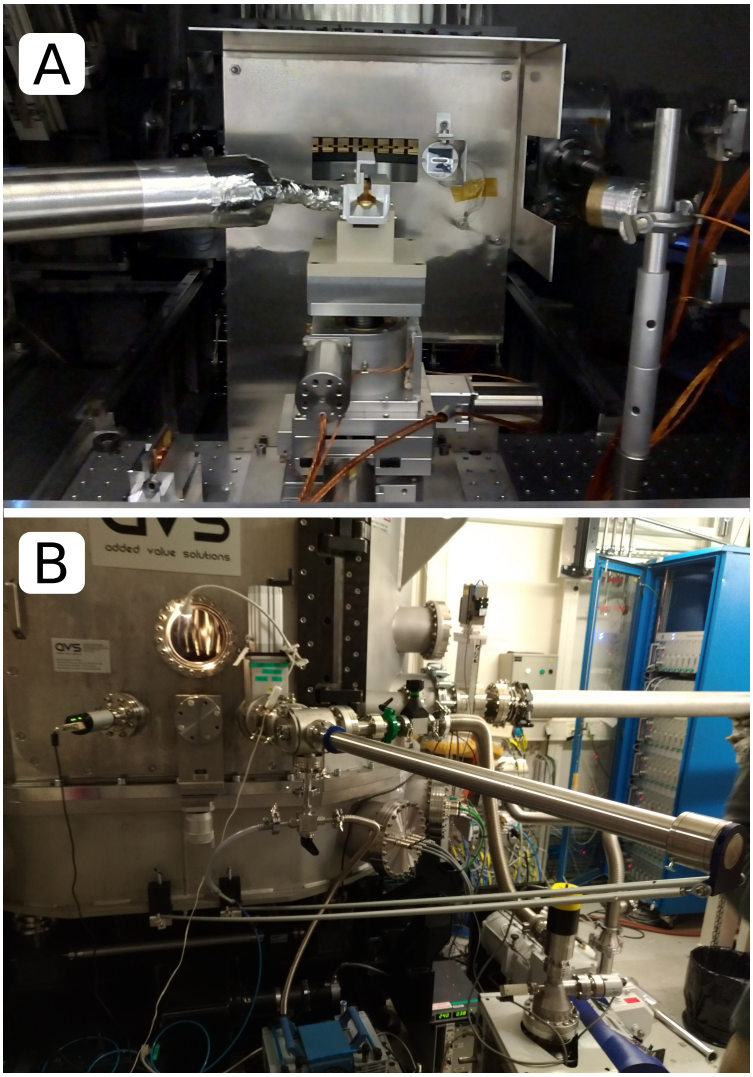

Figure S5. Sample environment space. Internal view (A): liquid He cryostat, shielding, sample tower, total fluorescence yield diodes. External view (B): load-lock system.

S8. MACHINING CYLINDRICAL JOHANSSON CRYSTAL ANALYSERS

The two standard machining approaches in the production of cylindrical Johansson crystal analysers, namely, single and double machining, are schematised in Figure S8.

S9. MEASURED EMISSION LINES

The measured emission lines reported in Table 1 of the main text are shown in Figure S9.

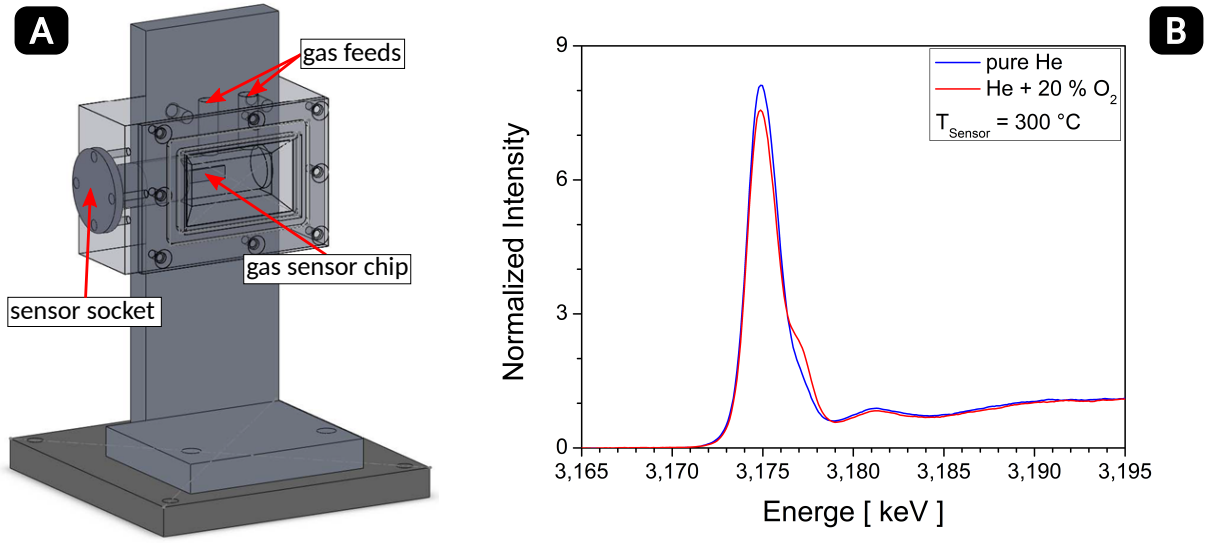

Figure S6. Schematic set-up of the operando XAS cell for gas sensors (A) and measurements at Pd L3-edge.

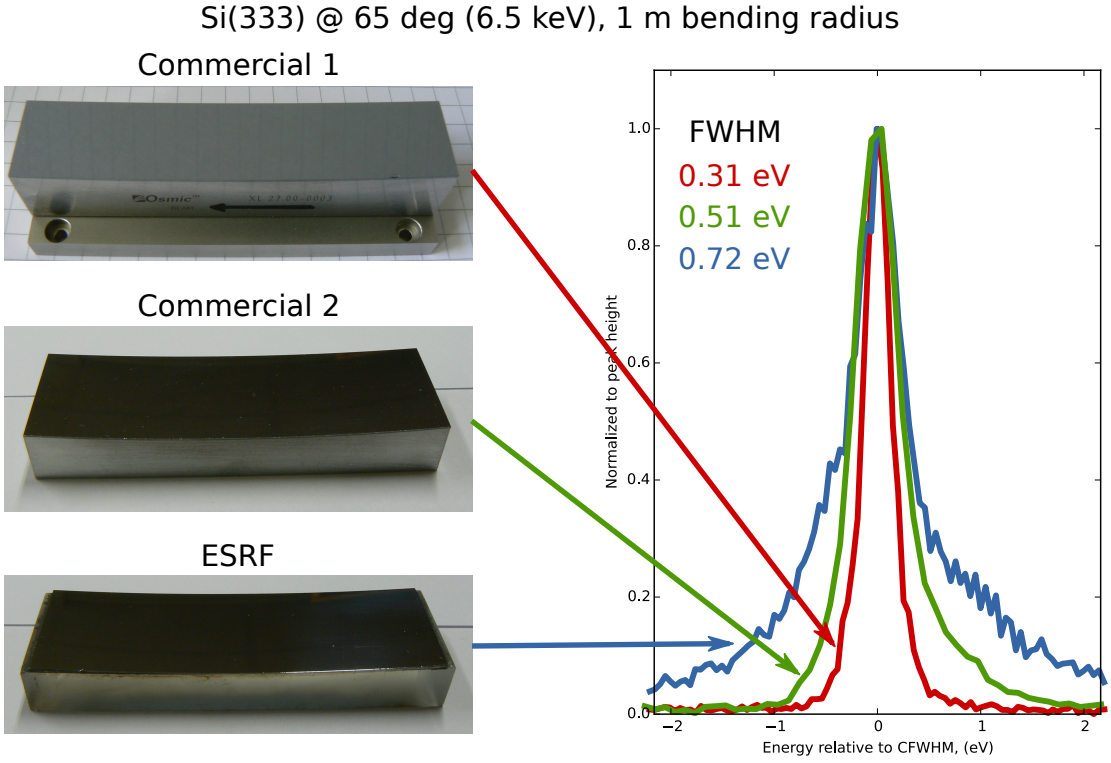

Figure S7. Initial characterisation of commercially available Johansson analysers versus one at the ESRF.

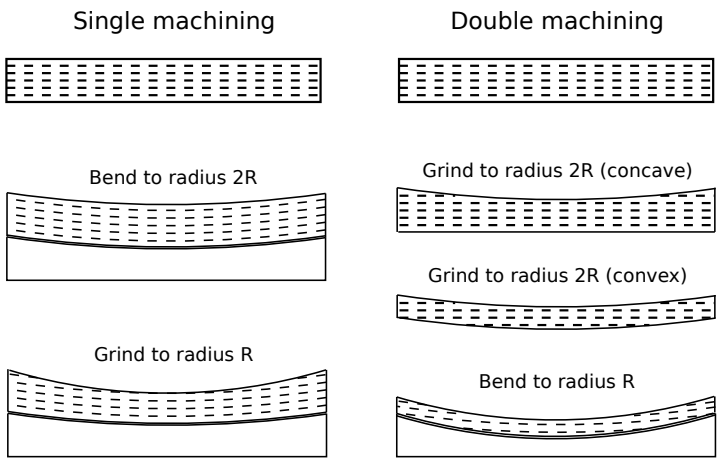

Figure S8. Machining approaches in Johansson crystal analysers production: single machining versus double machining. The dashed lines represent the atomic planes. Dimensions are not in scale.

S10. EXAMPLE OF PEAK FITTING

An example of peak the fitting for the S K$\alpha_{1,2}$ lines is shown in Figure S10. The signal of each wire of the gas detector is analysed independently and then the results merged in order to have an estimation of the standard deviation. Analysing each wire independently, has the advantage to catch any misalignment issues. The distribution of the plots is from the central wires (g12, g04) to the side ones (g07, g15). The two rows of wires are symmetrically distributed.

S11. BEST RADIUS OPTIMISATION PROCEDURE

The procedure employed for finding the best bending radius parameter (R) for each analyser is summarised in Figure S11.

REFERENCES

[S1]W. Zhao and K. Sakurai, Review of Scientific Instruments **88**, 063703 (2017).

[S2]L. Strüder, Nuclear Instruments and Methods in Physics Research Section A: Accelerators, Spectrometers, Detectors and Associated Equipment **454**, 73 (2000).

[S3]D. Doering, Y.-D. Chuang, N. Andresen, K. Chow, D. Contarato, C. Cummings, E. Domning, J. Joseph, J. S. Pepper, B. Smith, G. Zizka, C. Ford, W. S. Lee, M. Weaver, L. Patthey, J. Weizeorick, Z. Hussain, and P. Denes, Review of Scientific Instruments **82**, 073303 (2011).

[S4]I. Hafizh, G. Bellotti, M. Carminati, G. Utica, M. Gugiatti, A. Balerna, V. Tullio, G. Lepore, G. Borghi, F. Ficorella, A. Picciotto, N. Zorzi, A. Capsoni, S. Coelli, L. Bombelli, and C. Fiorini, Journal of Instrumentation **14**, P06027 (2019).

[S5]J. Bufon, M. Ahangarianabhari, P. Bellutti, G. Bertuccio, S. Carrato, G. Cautero, S. Fabiani, G. Giacomini, A. Gianoncelli, D. Giuressi, M. Grassi, P. Malcovati, R. Menk, A. Picciotto, C. Piemonte, I. Rashevskaya, A. Rachevski, A. Stolfa, A. Vacchi, G. Zampa, and N. Zampa, Journal of Instrumentation **9**, C12017 (2014).

[S6]T. Donath, S. Brandstetter, L. Cibik, S. Commichau, P. Hofer, M. Krumrey, B. Lüthi, S. Marggraf, P. Müller, M. Schneebeli, C. Schulze-Briese, and J. Wernecke, Journal of Physics: Conference Series **425**, 062001 (2013).

[S7]I. Klačková, G. Blaj, P. Denes, A. Dragone, S. Göde, S. Hauf, F. Januschek, J. Joseph, and M. Kuster, Journal of Instrumentation **14**, C01008 (2019).

[S8]W. M. Holden, O. R. Hoidn, G. T. Seidler, and A. D. DiChiara, Review of Scientific Instruments **89**, 093111 (2018).

[S9]M. S. Haro, F. A. Bessia, M. Pérez, J. J. Blostein, D. F. Balmaceda, M. G. Berisso, and J. Lipovetzky, Radiation Physics and Chemistry , 108354 (2019).

[S10]N. BARSAN, D. KOZIEJ, and U. WEIMAR, Sensors and Actuators B: Chemical **121**, 18 (2007).

[S11]D. Degler, Sensors **18**, 3544 (2018).

[S12]D. Degler, S. Rank, S. Müller, H. W. Pereira de Carvalho, J.-D. Grunwaldt, U. Weimar, and N. Barsan, ACS Sensors **1**, 1322 (2016).

[S13]M. Hübner, D. Koziej, M. Bauer, N. Barsan, K. Kvashnina, M. D. Rossell, U. Weimar, and J.-D. Grunwaldt, Angewandte Chemie International Edition **50**, 2841 (2011).

[S14]O. V. Safonova, T. Neisius, A. Ryzhikov, B. Chenevier, A. M. Gaskov, and M. Labeau, Chemical Communications , 5202 (2005).

[S15]D. Koziej, M. Hübner, N. Barsan, U. Weimar, M. Sikora, and J.-D. Grunwaldt, Physical Chemistry Chemical Physics **11**, 8620 (2009).

[S16]A. Staerz, I. Boehme, D. Degler, M. Bahri, D. Doronkin, A. Zimina, H. Brinkmann, S. Hermann, B. Junker, O. Ersen, J.-D. Grunwaldt, U. Weimar, and N. Barsan, Nanomaterials **8**, 892 (2018).

[S17]N. Barsan and U. Weimar, Journal of Physics: Condensed Matter **15**, R813 (2003).

[S18] M. Rovezzi, C. Lapras, A. Manceau, P. Glatzel, and R. Verbeni, Review of Scientific Instruments **88**, 013108 (2017).

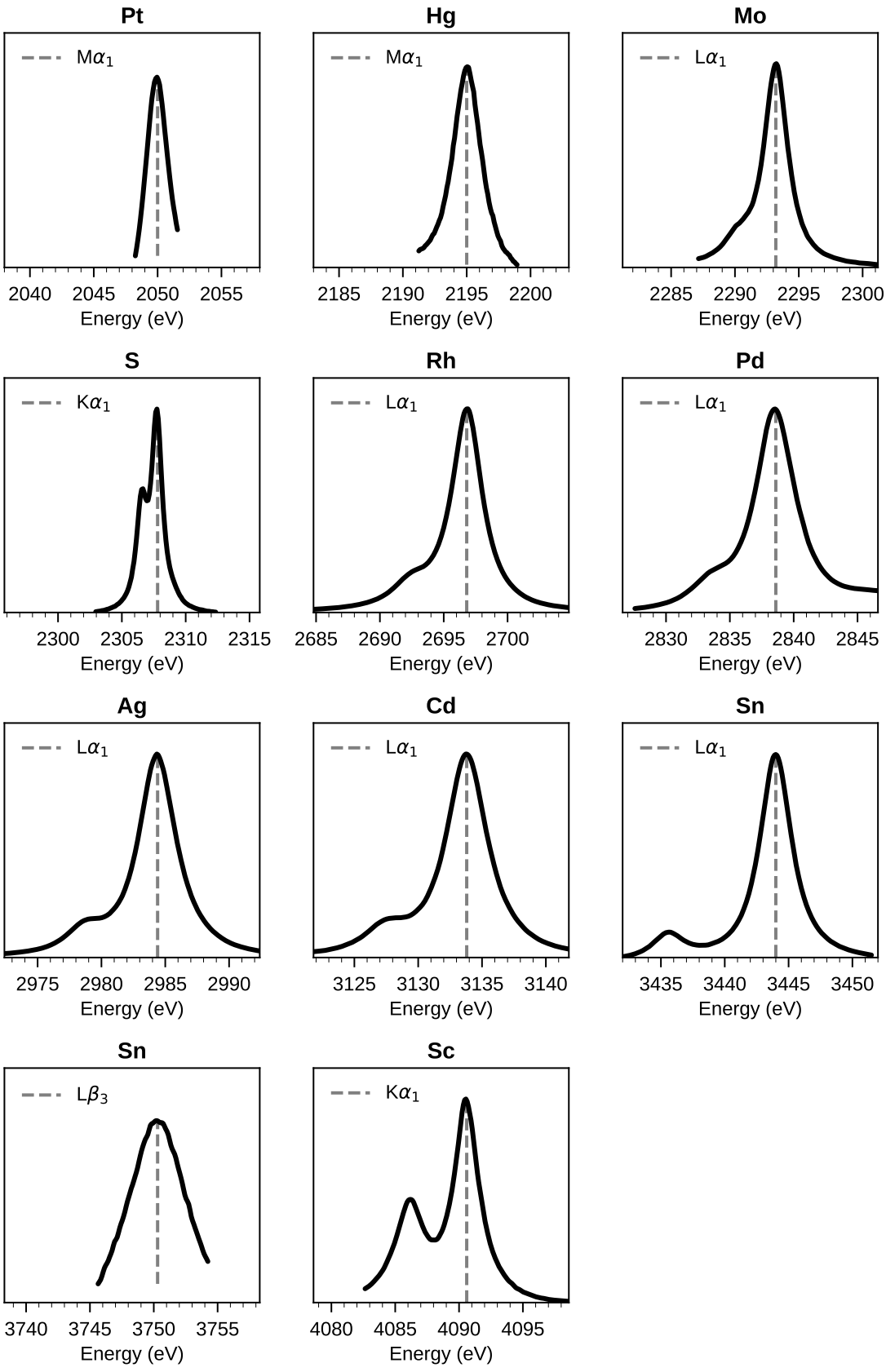

Figure S9. Measured emission lines. The energy range of all the plots is 20 eV.

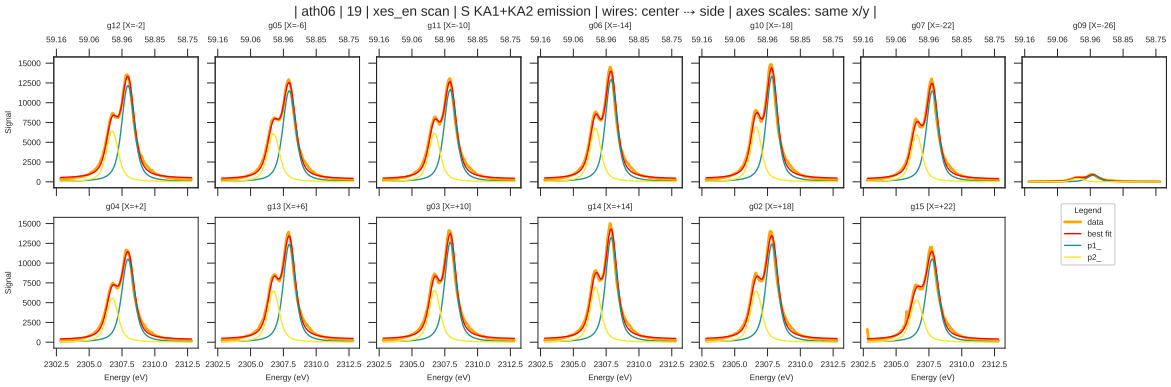

Figure S10. Peak fitting example for S K$\alpha_{1,2}$ lines.

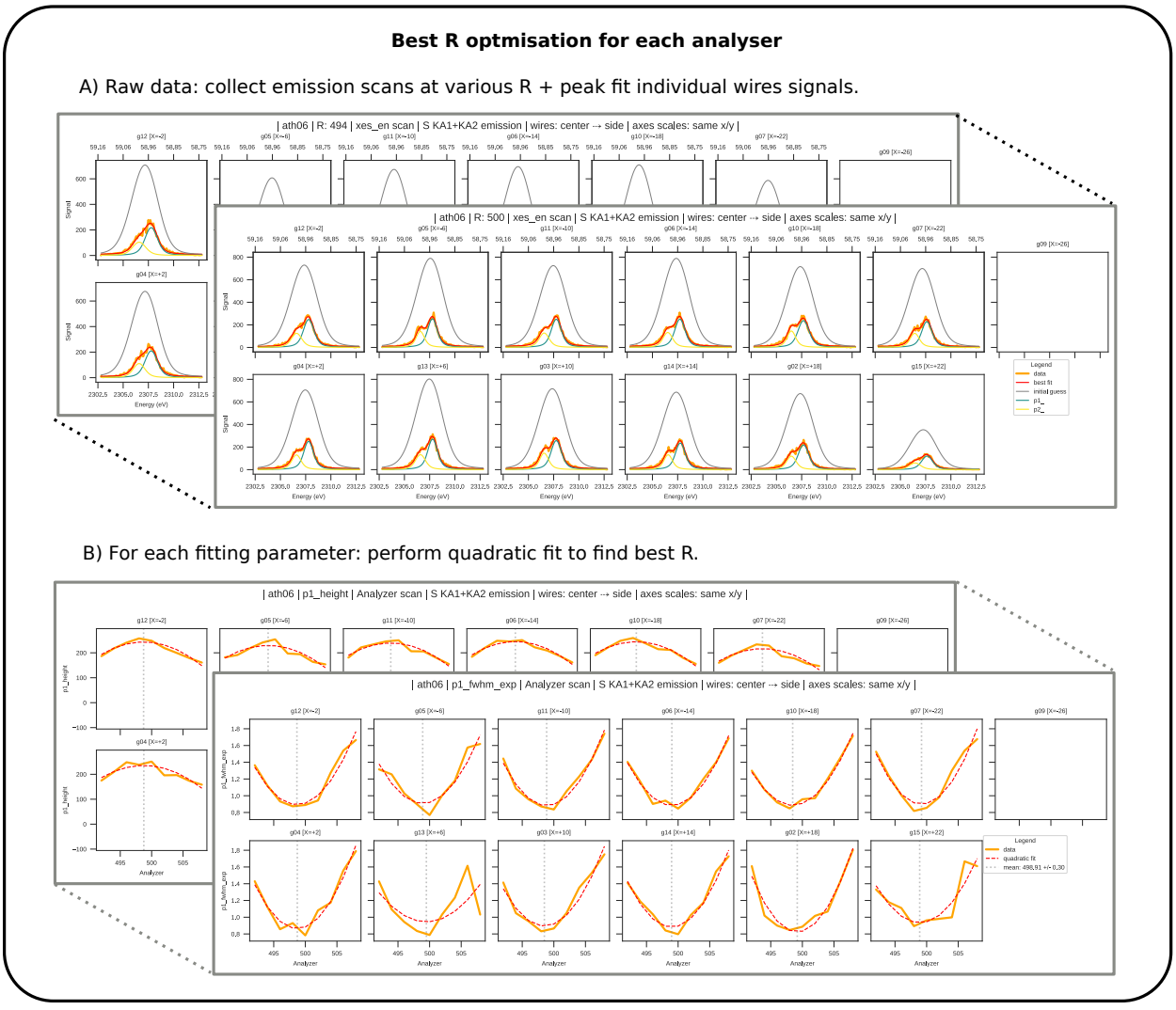

Figure S11. Procedure for finding the best bending radius (R) for each crystal. Here the example of Sulphur K$\alpha_{1,2}$ lines at around 59° Bragg angle with Si(111) single machining Johansson analysers is shown.